Palaeogeography, Palaeoclimatology, Palaeoecology 308 (2011) 65–83

Contents lists available at ScienceDirect

Palaeogeography, Palaeoclimatology, Palaeoecology

journal homepage: www.elsevier.com/locate/palaeo

Spatial variation in sediment fluxes, redox conditions, and productivity in the Permian–Triassic Panthalassic Ocean

Thomas J. Algeo [a,*], Kiyoko Kuwahara [b], Hiroyoshi Sano [c], Steven Bates [d], Timothy Lyons [d], Erika Elswick [e], Linda Hinnov [f], Brooks Ellwood [g], Jessa Moser [a], J. Barry Maynard [a]

[a] Department of Geology, University of Cincinnati, Cincinnati, OH 45221-0013, USA
[b] Faculty of Clinical Education, Ashiya University, Ashiya 659-8511, Japan
[c] Department of Earth and Planetary Sciences, Kyushu University, Fukuoka 812-8581, Japan
[d] Department of Earth Sciences, University of California, Riverside, California 92521-0423, USA
[e] Department of Geological Sciences, Indiana University, Bloomington, IN 47405-1405, USA
[f] Department of Earth and Planetary Sciences, Johns Hopkins University, Baltimore, MD 21218, USA
[g] Dept. of Geology and Geophysics, Louisiana State University, Baton Rouge, LA 70803, USA

ARTICLE INFO

Article history:
Received 13 January 2010
Received in revised form 22 April 2010
Accepted 9 July 2010
Available online 16 July 2010

Keywords:
Chert
Black shale
Primary productivity
Radiolarians
Mass extinction
Sediment geochemistry
Japan

ABSTRACT

Two Permian/Triassic boundary sections in central Japan provide a rare window into environmental conditions within the Panthalassic Ocean, which encompassed more than half the Earth's surface at 252 Ma. Integration of petrographic, geochemical, and time series data provides new insights regarding the fluxes of major and trace components to the sediment as well as environmental conditions in both the deep and intermediate water masses at each study site. The Ubara section was located in a high-productivity peri-equatorial location, whereas the Gujo-Hachiman section was located in a moderate-productivity location at some distance from the paleoequator. An upward transition from gray organic-poor cherts to black siliceous mudstones at both sites occurred in conjunction with increased primary productivity, intensified euxinia within the oxygen-minimum zone (OMZ), and decimation of the radiolarian zooplankton community. Euxinia in the OMZ of the equatorial Panthalassic Ocean developed episodically for a ~200–250 kyr interval during the Late Permian, followed by an abrupt intensification and lateral expansion of the OMZ around the Permian–Triassic boundary. Throughout the study interval, bottom waters at both sites remained mostly suboxic, a finding that counters hypotheses of development of a “superanoxic” Permo-Triassic deep ocean as a consequence of stagnation of oceanic overturning circulation.

1. Introduction

The Permian/Triassic boundary (PTB) mass extinction at ~252 Ma was the largest biotic catastrophe of the Phanerozoic Eon, resulting in the disappearance of ~90% of marine species as well as a large fraction of terrestrial taxa (Erwin, 1994; Bambach et al., 2004). The cause of this event has long been debated, and various hypotheses have been proposed, including a meteorite impact, flood basalt volcanism, global oceanic anoxia, and long-term climate change (Hallam and Wignall, 1997; Wignall, 2007). Recent research has demonstrated that many shallow-marine platforms of Late Permian and Early Triassic age experienced euxinic conditions, i.e., a lack of dissolved oxygen along with free H_2S in the water column (Nielson and Shen, 2004; Grice et al., 2005; Wignall et al., 2005; Riccardi et al., 2006; Algeo et al., 2008; Cao et al., 2009). The majority of these studies have been undertaken on sections from the Tethys Ocean, a region that comprised only 10–15% of the area of the global ocean and that formed an equatorial cul-de-sac acting as a nutrient trap, resulting in generally high levels of primary productivity and benthic oxygen demand (Winguth and Maier-Reimer, 2005; Virgili, 2008).

Environmental conditions in the larger Panthalassic Ocean, comprising 85–90% of the area of the Permian–Triassic global ocean, are more poorly known owing to later subduction of most oceanic crust of that age. The only surviving marine strata from the Panthalassic Ocean (as opposed to restricted continent-margin basins) are now located within accretionary terranes in Japan, New Zealand, and western Canada (Kojima, 1989; Monger et al., 1991; Isozaki, 1997a). Studies of Permo-Triassic-age Panthalassic seamounts preserved in Japanese accreted terranes have shown that, in shallow-marine settings, light-gray skeletal packstones and wackestones gave way to a mixed assemblage of dark-colored, fine-grained microbialites and molluscan and oncoidal limestones during the Early Triassic (Sano and Nakashima, 1997; Musashi et al., 2001), recording a transient interval of environmentally hostile conditions, as in coeval Tethyan sections.

* Corresponding author.
E-mail address: thomas.algeo@uc.edu (T.J. Algeo).

0031-0182/$ – see front matter © 2010 Elsevier B.V. All rights reserved.
doi:10.1016/j.palaeo.2010.07.007

Environmental conditions in the deep Panthalassic Ocean during the Permo-Triassic have been the subject of some debate, owing to differing interpretations of the extant evidence. A number of sedimentologic and geochemical studies of Japanese abyssal sections have inferred strongly reducing (probably euxinic) conditions in Panthalassic bottom waters (Isozaki, 1994, 1997b; Suzuki et al., 1998; Kato et al., 2002; Matsuo et al., 2003), and such results have been used to infer widespread deep-ocean anoxia during the Late Permian to Early Triassic interval (Wignall and Twitchett, 1996, 2002) despite the limited geographic coverage of the available evidence. Other studies have questioned the persistence and duration of deep-water anoxia recorded by Japanese abyssal sections on the basis of ichnofabric and other data (Kakuwa, 1996, 2008; Algeo et al., 2010). In this study, we examine the petrography and geochemistry of two abyssal Permian–Triassic sections from central Japan in order to gain new insights on these issues. Although one of the sections (Gujo-Hachiman) was the subject of an earlier paper (Algeo et al., 2010), the present report extends work on this section through an analysis of sedimentation rates and fluxes and their significance for contemporaneous oceanographic changes. The present contribution also reports chemostratigraphic and sediment flux data for a second section (Ubara), contrasting it with Gujo-Hachiman in order to assess spatial patterns of environmental variation within the Late Permian–Early Triassic Panthalassic Ocean.

2. Study sections

2.1. Geologic setting and paleogeography

The two study sections, Gujo-Hachiman and Ubara, are located in the Mino and Tanba belts, respectively, and are separated by a distance of ~160 km (Fig. 1A). The two belts are largely equivalent, being located in adjoining areas of central Japan and exhibiting strong similarities in their structure, ages, and tectonostratigraphic histories. The belts represent a subduction-generated accretionary complex consisting chiefly of Permian to Jurassic oceanic assemblages and Jurassic terrigenous clastics (Isozaki, 1997a). The Tanba and Mino belts are thought to have had the same travel history (Mizutani, 1987; Matsuda and Isozaki, 1991), although their timing of accretion varies slightly: Late Triassic to earliest Cretaceous for the Tanba Belt versus Early Jurassic to earliest Cretaceous for the Mino Belt. Both belts experienced regional low-grade metamorphism (prehnite–

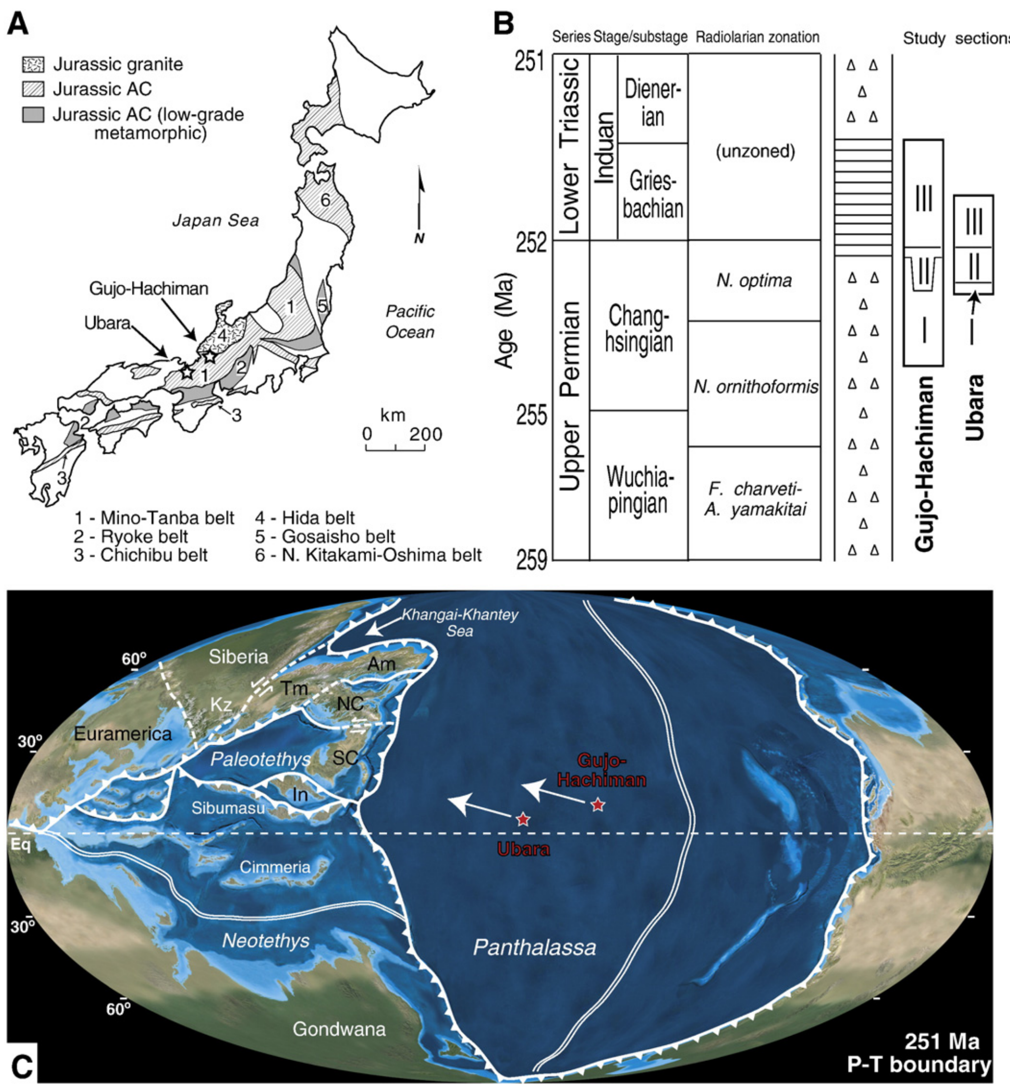

Fig. 1. Gujo-Hachiman and Ubara study sections: (A) location map, and (B) stratigraphy, including lithostratigraphic units I–III (modified from Kuwahara and Yao, 2001). (C) Global paleogeography at ~252 Ma. Abbreviations: Am = Amuria, In = Indonesia, Kz = Kazakhstan, NC = North China, SC = South China, and Tm = Tarim. Base map courtesy of Ron Blakey (http://jan.ucc.nau.edu/~rcb7/); plate boundaries adapted from Scotese and Langford (1995) and Stampfli and Borel (2001); location of Japanese terranes from Mizutani (1987) and Ando et al. (2001).

pumpellyite to lower greenschist facies) within 10 to 20 Myr of accretion (Isozaki, 1997a; Nakajima, 1997).

The PTB siliceous rocks examined in this paper (Fig. 1B) crop out as a laterally discrete, lenticular-shaped block in a Middle Jurassic mélange designated as Funabuseyama Unit by Wakita (1984, 1988). Its oceanic-rock assemblage includes Permian basaltic rocks, limestone, and ribbon-chert and related siliceous claystone, and Lower Triassic to Middle Jurassic ribbon-chert, all chaotically mingled with the matrix of pervasively and penetratively sheared, Middle Jurassic argillite. Tanba Belt rocks of the Ayabe area represent a Jurassic-age mélange termed the Wachi Complex and comprised of blocks of basaltic rocks, Permian to Triassic ribbon-chert and related siliceous rocks, sandstone, and minor Permian limestone, all chaotically embedded in the matrix of Middle Jurassic argillaceous rocks. The present study was undertaken on sheet-shaped blocks of Permo-Triassic cherts and associated siliceous claystones within this mélange (Fig. 1B).

During the Permo-Triassic, the study sites were located in the equatorial Panthalassic Ocean at a considerable distance from the eastern margin of the Pangean supercontinent (Fig. 1C). Paleomagnetic studies of Middle Triassic to Lower Jurassic cherts in central Japan have consistently yielded near-equatorial paleolatitudes, i.e., within 10° of the equator (Shibuya and Sasajima, 1986; Ando et al., 2001). Between the Late Triassic and Middle to Late Jurassic, Panthalassic Ocean crust was translated rapidly in a northwestward direction prior to subduction or accretion. Paleogeographic reconstructions show different latitudes for the Japanese terranes at the time of accretion: Isozaki (1997a) placed them at mid- to high northern hemisphere latitudes (~60–70°N), whereas Ando et al. (2001) inferred accretion at low latitudes (~10–20°N) followed by northward translation during the Cretaceous–Recent to their present positions (~35–40°N). The distance that these terranes traveled prior to accretion is not known with certainty, but a rough estimate of 3000–6000 km can be made on the basis of a 100-Myr travel history (i.e., mid-Triassic to Late Jurassic) and a convergence rate of 3–6 cm yr^{-1}. This estimate puts the Japanese terranes roughly in the middle of the Panthalassic Ocean during the Triassic (Fig. 1C).

2.2. Stratigraphy of Gujo-Hachiman

The Gujo-Hachiman section is located at 35.7355°N and 136.8489°E in the Gifu Prefecture of central Japan. Strata in this area are steeply dipping and cut by faults at several levels. Samples for the present study were collected from two internally conformable stratigraphic intervals that were offset along a shear fault (located at ~4.1 m in the measured section); the two intervals (GA and GC) were correlated carefully based on field relations and radiolarian zonation (Kuwahara, 1997). In aggregate, the study section is 7.65 m thick and comprises three lithostratigraphic units. The lowermost unit (I) consists of green–gray ribbon-chert and is more than 9 m thick; the upper ~7.0 m was examined in the present study (Fig. 2A). Unit II consists of green–gray siliceous claystone and is ~25 cm thick (Fig. 2B). The uppermost unit (III) consists of black siliceous mudstone ("black shale" for short) and is more than 1 m thick, but only the lower ~65 cm was examined in the present study. The lowermost 40 cm of unit III contains a few thin lenses of gray chert and layers of white–yellow siliceous claystone bearing uppermost Permian radiolarians; the upper part of this unit consists entirely of black shale (Fig. 2B).

Placement of the PTB in the Gujo-Hachiman section is uncertain owing to limited biostratigraphic age control. Radiolarians of Changxingian age have been recovered from units I and II and

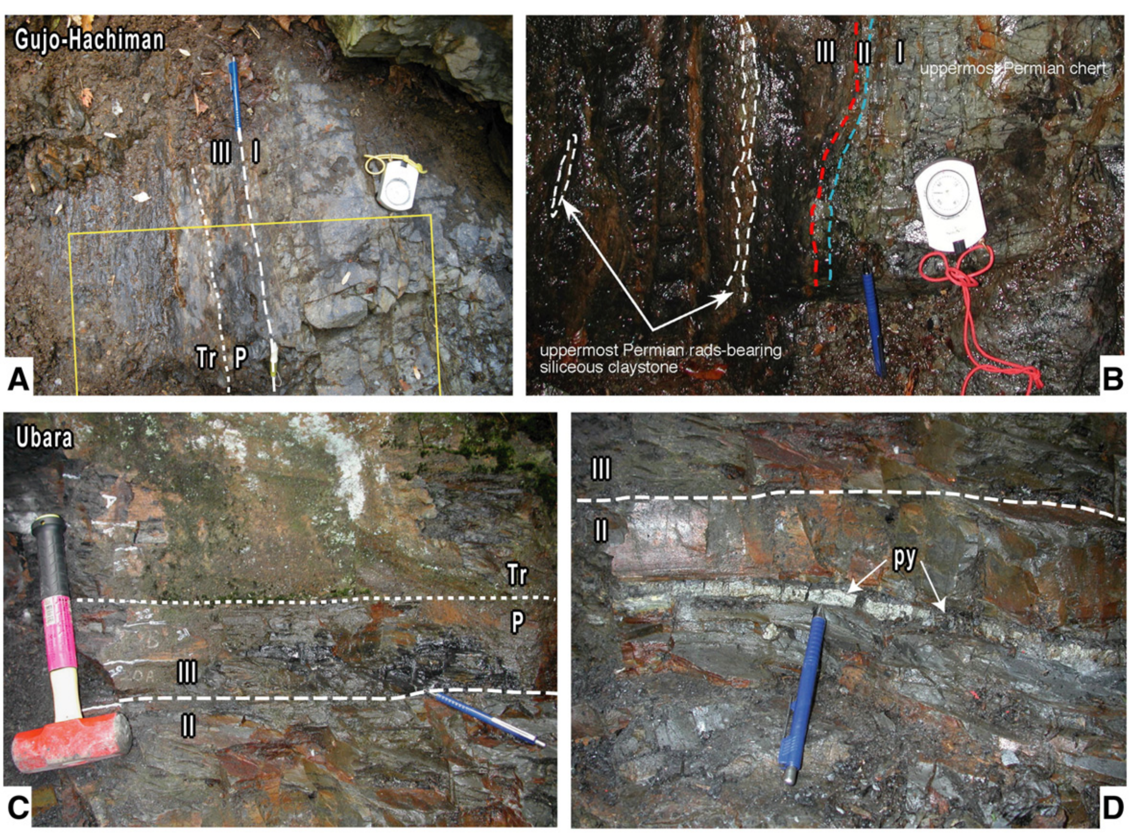

Fig. 2. Field photos of Gujo-Hachiman (A–B) and Ubara (C–D). Shown are contacts between the chert and black shale facies (long-dashed lines), the approximate position of the Permian (P)–Triassic (Tr) boundary (short-dashed lines), and lithostratigraphic units I–III (see text). The area of the close-up view in photo B is shown by the yellow rectangle in photo A; dashes enclose lenses of radiolarian-bearing siliceous claystone enclosed in a black shale matrix. Photo D shows the 2-cm-thick massive pyrite (py) layer in the uppermost part of the chert facies at Ubara.

siliceous claystone lenses/layers in the lower part of the black shale (unit III), e.g., *Albaillella triangularis* and *Neoalbaillella* sp. from 10 cm above the unit base and *Neoalbaillella* sp. from 30 cm above the unit base (Kuwahara et al., 1991; Kuwahara and Yao, 2001; Yao et al., 2001). However, the black shale matrix of unit III has yielded no radiolarians or conodonts, either from the basal 40 cm containing siliceous claystone lenses/layers or from the overlying chert-free section, despite attempts at recovery by Drs. Satoshi Yamakita and Kiyoko Kuwahara. The age significance of the radiolarians from the siliceous claystone lenses/layers in the basal portion of unit III is open to question. Permian-type radiolarians have been reported from black shale facies of possible Lower Triassic age in several locales, e.g., Mino Terrane, Japan (Sugiyama, 1992), Russia (Bragin, 1991), South China (Yao et al., 2005), and New Zealand (Takemura et al., 2007). The interpretation of these finds has varied: Sugiyama (1992) inferred reworking of Upper Permian fossils into Lower Triassic beds, but Takemura et al. (2007) inferred survival of some Late Permian radiolarians into the Early Triassic. If either of these processes operated at Gujo-Hachiman, then the basal 30 cm of the black shale facies (unit III) would be Early Triassic in age, rather than latest Permian. Elsewhere in Japan, the guide fossil for the base of the Triassic, *Hindeodus parvus*, has been identified near the base of black shale units straddling the PTB (Yamakita et al., 1999). These considerations suggest, but do not prove, that the PTB lies near the base of the black shale facies (unit III) at Gujo-Hachiman (Fig. 2A-B). Dienerian- to Spathian-age conodonts have been recovered from chert beds overlying unit III, although these younger beds are in fault contact with unit III and thus not demonstrably conformable (Yamakita, 1987).

2.3. Stratigraphy of Ubara

The Ubara section is located at 35.189896 N, 135.2515E, near the village of Ubara in the Ayabe area (Kyoto Prefecture) of central Japan (Kimura et al., 1989). The section is nearly flat-lying although cut by faults at several levels; samples for the present study were collected from a portion of the outcrop that was fault-free and consisted of a conformable succession of beds straddling the Permian–Triassic boundary (Kuwahara et al., 1991; Yamakita et al., 1999). The study section is 135 cm thick and comprises three lithostratigraphic units (Fig. 2C). The lowermost unit (I) consists of gray bedded cherts and is more than 3 m thick, but only the uppermost ~10 cm was examined in this study. Unit II consists of alternating beds of gray chert and black shale and is ~1 m thick. The latter facies contains abundant pyrite nodules and lenses, including a prominent 2- to 3-cm-thick layer of massive pyrite ~10 cm below its upper contact (Fig. 2D). The uppermost unit (III) consists entirely of black shale and is more than 1 m thick, but only the lowermost ~25 cm was examined in this study. Units I–III are unlikely to be correlative between the two study sections; in particular, most of unit II at Ubara may be the stratigraphic equivalent of the upper part of unit I at Gujo-Hachiman. Sedimentation rates were similar for both sections (see Section 4.6), so the 7.5-m-thick Gujo-Hachiman section represents a ~5X longer depositional interval than the 140-cm-thick Ubara section.

The position of the PTB at Ubara has been narrowly constrained by studies of radiolarian (Kuwahara et al., 1991, 1998) and conodont biostratigraphy (Yamakita et al., 1999). Samples collected from unit I yielded specimens of the radiolarian *Neoalbaillella ornithoformis*, which suggests a mid-Late Permian age (Fig. 1B), but these cherts are in fault contact with our study section and, hence, not demonstrably conformable. The radiolarian *A. triangularis* was extracted from unit II (samples Ub-3-6 and Ub-3-7 in Kuwahara et al., 1991), which can therefore be assigned to the *Neoalbaillella optima* zone of latest Permian age, an age assignment confirmed by the presence of the conodont *Neogondolella changxingensis* (Yamakita et al., 1999). The conodont *H. parvus* was recovered from the lowermost part (~10 cm above the base) of unit III, demonstrating an earliest Triassic age for the bulk of the black shale facies (Yamakita et al., 1999). These observations constrain the position of the PTB to near the base of unit III.

3. Methods

A total of 101 samples from Gujo-Hachiman and 25 samples from Ubara were washed, dried at 110 °C, and trimmed to remove visible veins and weathered surfaces. Standard petrographic thin sections were prepared for a subset of samples from each section, from which pyrite size was determined at 20–400X magnification under reflected light using a Leitz Laborlux 12-Pol optical microscope calibrated with a Zeiss micrometer. Pyrite grain-size distributions were based on 300 point counts of each thin section using an equally spaced grid. The thin sections were also examined using a Hitachi scanning electron microscope (SEM) in the University of Cincinnati Materials Science Department to image finer petrographic details.

Magnetic susceptibility (MS) was measured using a high-sensitivity susceptibility bridge at Louisiana State University. The susceptibility bridge was calibrated using standard salts, for which values are given in Swartzendruber (1992) and the Handbook of Physics and Chemistry (2004). Reported MS values represent the mean of three measurements in units of $m^3\ kg^{-1}$.

For geochemical analysis, samples were ground in a SPEX 8000D mixer mill and pressed into pellets using a SPEX 3624B X-Press. Major- and trace-element concentrations were determined using a wavelength-dispersive Rigaku 3040 X-ray fluorescence spectrometer, and results calibrated using USGS and internal laboratory standards. Analytical precision was better than ±2% for major and minor elements and ±5% for trace elements. Carbon and sulfur elemental concentrations were determined using an Eltra 2000 C-S analyzer, and results calibrated using USGS and internal laboratory standards. Analytical precision was better than ±2.5% for carbon and ±5% for sulfur. An aliquot of each sample was digested in HCl at 50 °C for 12 h, washed and filtered, and reanalyzed for C and S in order to determine concentrations of total organic carbon (TOC) and non-acid volatile sulfur (NAVS).

Sulfur speciation was undertaken on a subset of 41 samples from Gujo-Hachiman and for all 25 samples from Ubara. The mono-sulfide and pyrite-sulfide phases were separated by wet chemical extraction and trapped as Ag_2S in a procedure modified from Canfield et al. (1986) as described in Brüchert (1998) and Lefticariu et al. (2006). The precipitated Ag_2S was analyzed at the Indiana University Stable Isotope Research Facility (IU SIRF) using a CE Instruments EA1110 CHN elemental analyzer that was re-configured for sulfur combustion, interfaced with a Finnigan MAT 252 isotopic ratio mass spectrometer. Sample analyses were standardized with NBS 127 and two internal laboratory standards to bracket the range of isotopic values observed, yielding estimated uncertainties of ±0.2‰. Values are reported in per mille (‰) relative to the Vienna Canyon Diablo Troilite (VCDT).

The mineral composition of the non-volatile fraction of the study section was calculated as follows:

$$\text{Illite}(\%) = \text{Al}_{\text{meas}} \times 100 / \kappa_1 \tag{1}$$

$$\text{Chert}(\%) = \text{SiO}_{2(\text{meas})} - (\text{Al}_{\text{meas}} / 27 \times \kappa_2 \times 60.1). \tag{2}$$

Eqs. (1) and (2) are formulas for calculating model amounts of illite and chert (or quartz) in a sample based on measured Al and SiO_2 concentrations. The coefficients 12, 27, and 60.1 represent the molar weights in grams of C, Al, and SiO_2, respectively. Coefficients κ_1 and κ_2 represent the average concentration of Al and the average molar Si:Al ratio, respectively, for a suite of illite samples of diverse provenance (data from Grim, 1968). Values of 12.0 for κ_1 and 2.14 for κ_2 were found to yield an average two-component sum equal to 100%-LOI (the loss on ignition, representing the volatile fraction of the sample) with a standard deviation of 1.6% for the sample set as a whole. Where deviating from unity, the three-component sums for individual samples were normalized to 100%.

Pyrite Fe (Fe_{py}) and non-pyrite Fe (Fe_{non}) were calculated as:

$$Fe_{py} = S_{total} \times 55.85 / 64.16 \quad (3)$$

$$Fe_{non} = Fe_{total} - Fe_{py} \quad (4)$$

where 55.85 and 64.16 are the molar weights of Fe and S in stoichiometric pyrite (FeS_2), and total S was used as a proxy for pyrite S (a good first approximation in view of the low concentrations of organic matter and, hence, organic-bound S in the study samples).

Time series analysis was carried out on the study sections, which showed evidence of cyclicity at timescales of 10^4–10^6 yr. Although the original samples were collected at irregular intervals mostly between 5 and 10 cm, the geochemical data series were resampled to yield a high-resolution even spacing through linear interpolation, taking care to note the original Nyquist frequency range. Multitaper spectral analysis was applied using Analyseries (Paillard et al., 1996), along with evolutionary spectrogram analysis (magnitude-squared FFT moduli) to examine cycle content and frequency as well as evidence for variable accumulation rates (changes in frequency).

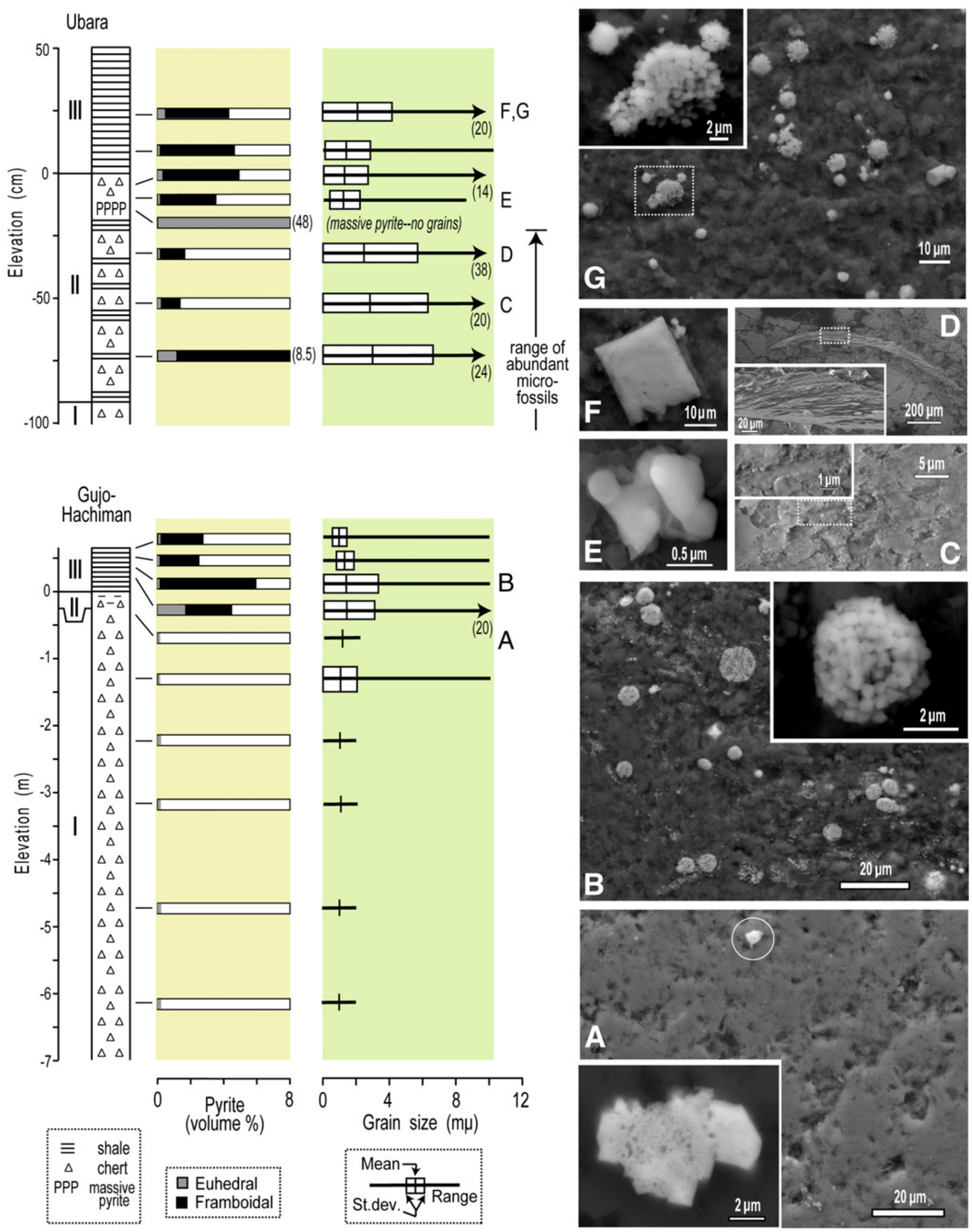

Fig. 3. Petrography of Gujo-Hachiman (below) and Ubara (above), showing generalized stratigraphy including lithostratigraphic units I–III (left), pyrite abundance by grain type (center–left), and pyrite grain size (center–right). SEM photos (right) show representative samples for Gujo-Hachiman (A–B) and Ubara (C–G); stratigraphic positions of photos shown by corresponding letters to left. (A) Euhedral pyrite (circled) in chert facies; (B) framboidal pyrite in black shale facies; (C–D) microfossils in chert facies (note range shown to left); (E) euhedral pyrite with sulfate overgrowth; and (F) euhedral pyrite and (G) framboidal pyrite in black shale facies. Locations of high-magnification insets in C, D, and G shown by dotted rectangles. The vertical axis in this and subsequent figures is scaled relative to the unit II–unit III contact in each study section.

4. Results

4.1. Petrography

The study sections are comprised largely of two lithofacies, gray chert and black shale (Fig. 3). The chert facies consists of microcrystalline quartz in a densely intergrown matrix and contains a variety of microfossils, including abundant radiolarians. The matrix contains minute particles of carbonaceous matter, which are locally condensed to form discrete seams and laminae. Microfossils are abundant throughout unit I at Gujo-Hachiman and units I and II of Ubara up to the level of the massive pyrite layer (Fig. 3C–D). The black shale facies consists of a groundmass of clay minerals and microcrystalline quartz. The groundmass looks cloudy due to a diffuse admixture of extremely fine-grained, black carbonaceous matter. Organic matter in both study sections consists entirely of structureless amorphous kerogen (Fig. 3; cf. Suzuki et al., 1998). This material is of marine algal origin although with some fraction of bacterial biomass. No organic matter of higher terrestrial plant origin was identified.

Pyrite is present in small quantities in the chert facies: <1% at Gujo-Hachiman and 2–6% at Ubara (by volume). At Gujo-Hachiman, these grains are entirely euhedral and mostly of small size (<2 μm; Fig. 3A). At Ubara, pyrite in the chert facies consists mainly of small (<2 μm) framboids. In both sections, pyrite shows marked changes in morphology, size, and isotopic composition from the chert to the black shale facies. At Gujo-Hachiman, pyrite comprises 3–7% of the latter facies and framboids become dominant, accounting for ~60–90% of all pyrite grains (Fig. 3B). At Ubara, pyrite comprises 4–10% of the black shale facies and framboids constitute ~90–95% of all pyrite grains (Fig. 3G). In both sections, these framboids have diameters of 5–10 μm, whereas co-occurring euhedral grains tend toward much larger sizes (to 250 μm; Fig. 3F). Many pyrite grains show overgrowths of gypsum (Fig. 3E), which probably account for the presence of measurable quantities of an acid-soluble phase in some samples; all such gypsum occurrences probably represent weathering of pyrite in the near-surface environment. The S-isotopic composition of pyrite varies between facies as well. At Gujo-Hachiman, $\delta^{34}S_{py}$ averages $+0.5\pm26.0$‰ in the chert facies (n = 4) and -31.6 ± 6.2‰ (n = 19) in the black shale facies. At Ubara, $\delta^{34}S_{py}$ averages -27.4 ± 2.7‰ in the chert facies (n = 14) and -31.3 ± 5.5‰ (n = 11) in the black shale facies (Fig. 4H).

4.2. Magneto- and chemostratigraphy

The study sections exhibit distinct stratigraphic variation in major components. At Gujo-Hachiman, chert abundance decreases from 89 ± 5% in the chert facies to 51 ± 8% in the black shale facies (Fig. 4A). Concurrently, illite increases from 9 ± 5% to 44 ± 8% and other components (mainly organic matter and pyrite) increase from ~1–2% to ~4–5%. At Ubara, chert abundance decreases from 79 ± 8% in the chert facies to 57 ± 4% in the black shale facies (Fig. 4A). Concurrently, illite increases from 18 ± 8% to 38 ± 7% and other sediment components increase from ~2–3% to ~5–6%. The transition from gray cherts to black shales is more abrupt at Gujo-Hachiman, where it is largely confined to a few-centimeter-thick interval across the unit II–III contact, than at Ubara, where interbedding of chert and shale layers is found throughout the ~1-m-thick unit II. Cyclic variation in bulk lithology is evident at several length scales in both sections, but most prominently in the decimeter range (see Section 4.5).

The study sections exhibit a limited range of MS values, mainly between 10^{-8} and 10^{-7} $m^3\,kg^{-1}$, although with substantial sample-to-sample variability (Fig. 4B). At Gujo-Hachiman, the MS profile exhibits a shift toward lower values around −225 cm and becomes markedly less variable within the unit III. At Ubara, the MS profile does not reveal any long-term trend but shows a decrease in variability in the upper part of unit II and in unit III, similar to that observed in unit III at Gujo-Hachiman. Dm-scale cyclic variation in MS values is also evident.

Degree-of-pyritization (DOP; Raiswell et al., 1988) values show a close relationship to lithofacies in both study sections. At Gujo-Hachiman, DOP values are generally low (<0.2) in unit I (but transiently rise to ~0.70 at −1.4 m), intermediate (0.2–0.4) in unit II, and high (mostly 0.4–0.7) in unit III (Fig. 4D). At Ubara, DOP values show a smaller total range of variation and smaller differences between stratigraphic units. All three units yield values between 0.4 and 0.75 (with a few outliers) with substantial sample-to-sample variability (Fig. 4D).

Lithofacies variation within the study sections is mirrored closely by changes in sediment chemistry. At Gujo-Hachiman, average Al concentrations increase from 1.1 ± 0.6% in the chert facies to 5.2 ± 0.9% in the black shale facies (Fig. 4C), i.e., by a factor of 4.82X (Table 1, col. C). Increases of similar magnitude (~4–5X) are shown by other elements associated dominantly with the detrital fraction (K, Mg, and Ti) as well as by some metals (Co, Zn, and Ni; Table 1). TOC increases from 0.2 ± 0.1% in the chert facies to 1.2 ± 0.5% in the black shale facies (Fig. 4E), i.e., by a factor of 6.45X (Table 1). Slightly larger increases (~7–8X) are shown by a group of redox-sensitive trace metals, including Mo, V, and U (Fig. 4F; Table 1). S increases from 0.1 ± 0.1% in the chert facies to 1.6 ± 0.6% in the black shale facies (Fig. 4G), i.e., by a factor of 30.4X, far exceeding that of other analyzed elements (Table 1). The remaining elements (P, Fe, Ba, and Si) exhibit variable changes from the chert to the black shale facies (Table 1).

Normalization of elemental concentration data to Al (Table 1, col. D) allows changes in the degree of authigenic enrichment (or depletion) between the chert and black shale facies to be assessed. At Gujo-Hachiman, the Al-normalized concentration ratios of K, Mg, and Ti are all close to 1.0, confirming association of these elements predominantly with the detrital fraction (Fig. 5). The same may be true of non- or weakly redox-sensitive metals such as Co, Zn, and Ni. The Al-normalized ratios for TOC and for strongly redox-sensitive metals such as Mo, V, and U vary from 1.3X to 1.7X, indicating a modest increase in the accumulation of these elements in the black shale facies relative to the chert facies (Fig. 5). However, by far the largest increase (6.3X) is shown by S, reflecting a substantial increase in syngenetic pyrite (i.e., pyrite formed in the water column) to the sediment (Fig. 5). On an Al-normalized basis, P exhibits little variation between facies (0.97X), but Fe, Ba, and total and biogenic SiO_2 exhibit decreases ranging from 0.39X to 0.12X (Table 1).

Similar facies-related changes in sediment chemistry are observed at Ubara, although with differences in detail. Al increases from 2.2 ± 1.0% in the chert facies to 4.5 ± 1.1% in the black shale facies (Fig. 4C), i.e., by a factor of 2.05X (Table 2, col. C). Increases of similar magnitude (1.3–2.3X) are shown by other detrital elements (Mg, Ti, and K) and non- or weakly redox-sensitive metals (Co, Ni, and Zn; Table 2). TOC increases from 0.13 ± 0.06% in the chert facies to 0.52 ± 0.35% in the black shale facies (Fig. 4E), i.e., by a factor of 4.05X (Table 2). Somewhat larger increases (4.8X to 10.5X) are shown by strongly redox-sensitive metals such as U, Mo, and V (Fig. 4F; Table 2). S increases from 1.0 ± 0.9% in the chert facies to 4.8 ± 7.8% in the black shale facies (Fig. 4G), i.e., by a factor of 2.31X (Table 2). Other elements (P, Fe, Ba, and Si) exhibit variable changes from the chert to the black shale facies (Table 2).

Again, normalization of elemental concentration data to Al (Table 2, col. D) facilitates comparisons of authigenic enrichment (or depletion) of elements between the chert and black shale facies. At Ubara, the black shale facies is enriched relative to the chert facies in TOC and strongly redox-sensitive metals by factors of 1.97X to 10.5X, as well as in P (4.00X), S (2.31X), and Ba (2.07X; Fig. 5). Fe shows little change between facies (0.95X), whereas total SiO_2 exhibits a marked decrease (0.42X). The Al-normalized concentration ratios are also useful for making comparisons between the two study sections.

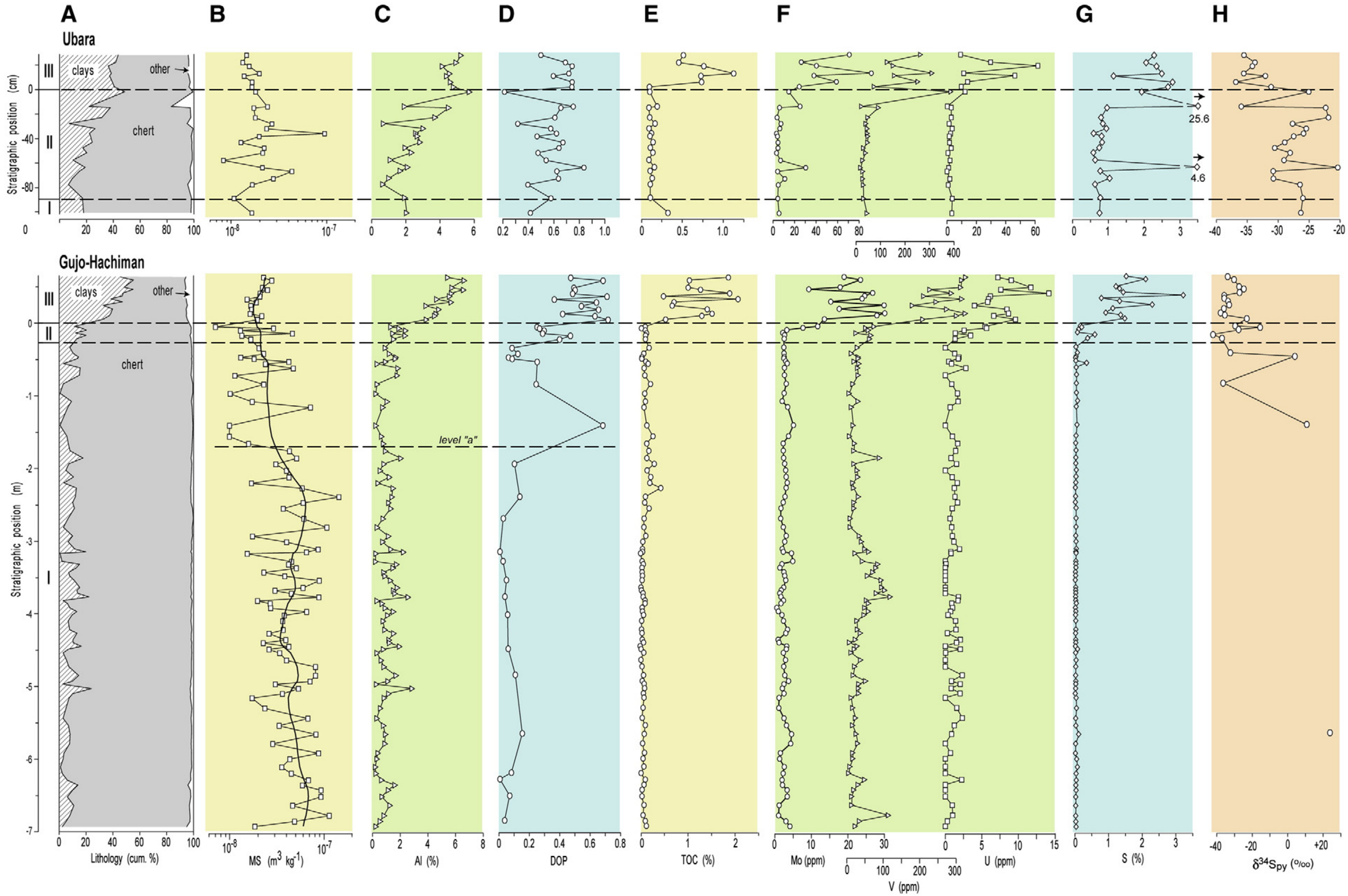

Fig. 4. Litho- and chemostratigraphy for Gujo-Hachiman (below) and Ubara (above): (A) lithology (calculated per Eqs. (1) and (2)), (B) magnetic susceptibility (heavy line is a weighted running average), (C) aluminum, (D) degree-of-pyritization, (E) total organic carbon, (F) molybdenum, vanadium, and uranium, (G) total sulfur, and (H) pyrite $\delta^{34}S$. Level "a" shows evidence of a perturbation in the MS and DOP records prior to the lithologic transition higher in the section.

Table 1
Gujo-Hachiman elemental concentrations and ratios.

	A	B	C	D
	Ch-avg[1]	BS-avg[1]	X $_{BS/Ch}$[2]	(X/Al) $_{BS/Ch}$[2]
S (%)	0.05	1.15	30.43	6.32
Mo (ppm)	2.7	21.5	8.06	1.67
U (ppm)	1.1	8.1	7.72	1.60
V (ppm)	37	272	7.25	1.50
TOC (%)	0.19	1.24	6.45	1.34
Al (%)	1.08	5.21	4.82	1.00
P (ppm)	118	555	4.71	0.97
Co (ppm)	4.0	17.7	4.49	0.94
K (%)	0.51	2.20	4.30	0.90
Mg (%)	0.25	1.05	4.26	0.89
Ti (%)	0.07	0.28	4.15	0.87
Zn (ppm)	30	122	4.05	0.85
Ni (ppm)	20	78	3.93	0.82
Fe (%)	1.52	2.82	1.86	0.39
Ba (ppm)	524	611	1.17	0.24
SiO_2-tot (%)[3]	92.4	74.0	0.80	0.17
SiO_2-bio (%)[3]	89.4	51.1	0.57	0.12

[1] Average elemental concentrations for the chert (Ch) and black shale (BS) units.
[2] Concentration ratios on a raw (X) and Al-normalized (X/Al) basis.
[3] SiO_2-tot = total SiO_2; SiO_2-bio = biogenic SiO_2 (i.e., chert; Eq. (2)).

Table 2
Ubara elemental concentrations and ratios.

	A	B	C	D
	Ch-avg[1]	BS-avg[1]	X $_{BS/Ch}$[2]	(X/Al) $_{BS/Ch}$[2]
U (ppm)	2.1	21.6	10.5	5.12
P (ppm)	172	1407	8.20	4.00
Mo (ppm)	6.9	43.3	6.27	3.06
V (ppm)	40	194	4.83	2.35
S (%)	1.02	4.81	4.74	2.31
Ba (ppm)	386	1644	4.25	2.07
TOC (%)	0.13	0.52	4.05	1.97
Co (ppm)	6.4	14.7	2.30	1.12
Al (%)	2.19	4.49	2.05	1.00
Mg (%)	0.43	0.88	2.05	1.00
Ti (%)	0.11	0.21	2.02	0.98
Fe (%)	2.70	5.24	1.94	0.95
K (%)	1.04	1.72	1.64	0.80
Ni (ppm)	33	47	1.43	0.70
Zn (ppm)	62	81	1.31	0.64
SiO_2-tot (%)[3]	87.3	74.9	0.86	0.42
SiO_2-bio (%)[3]	78.9	56.6	0.72	0.35

[1] Average elemental concentrations for the chert (Ch) and black shale (BS) units.
[2] Concentration ratios on a raw (X) and Al-normalized (X/Al) basis.
[3] SiO_2-tot = total SiO_2; SiO_2-bio = biogenic SiO_2 (i.e., chert; Eq. (2)).

Relative to Gujo-Hachiman, Ubara shows larger chert-to-black shale increases in TOC (1.97X vs. 1.34X) and strongly redox-sensitive metals (2.3–5.1X vs. 1.5–1.7X), but a smaller increase in S (2.31X vs. 6.32X) and smaller decreases in Fe (0.95X vs. 0.39X), total SiO_2 (0.42X vs. 0.17X), and biogenic SiO_2 (0.35X vs. 0.12X; Tables 1 and 2; Fig. 5). For other analyzed elements, the two study sections show dissimilar patterns of change from the chert to the black shale facies: P and Ba increase by 4.00X and 2.07X, respectively, at Ubara, but decrease by 0.97X and 0.24X at Gujo-Hachiman.

The general significance of these elemental patterns is that many differences in bulk chemistry between the chert and black shale facies of the two study sections can be accounted for through a sharp decrease in the flux of biogenic (radiolarian) silica during deposition of the latter facies (see Section 5.1). At Gujo-Hachiman, the decrease in biogenic SiO_2 abundance from the chert facies (89%) to the black shale facies (51%) corresponds to a 4.6X reduction in the sinking flux of this component, which is almost exactly the inverse of the 4–5X enrichments observed for detrital elements such as Al, Mg, K, and Ti (Table 1). These observations are consistent with a ~4X shift in the

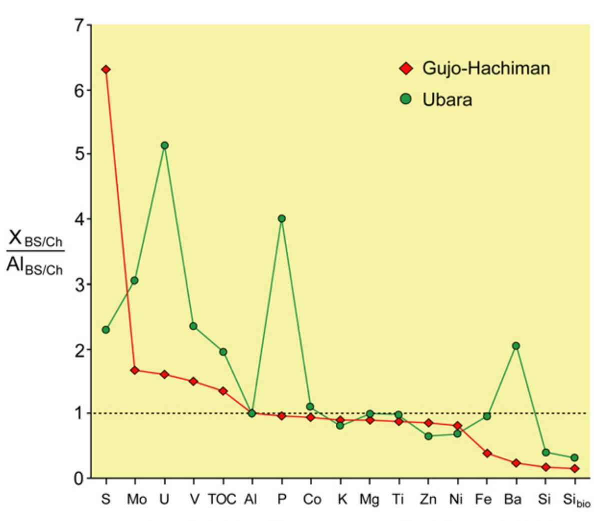

Fig. 5. Ratios of average elemental concentrations in the black shale-versus-chert facies on an Al-normalized basis (Tables 1 and 2, col. D) for both study sections. Elements ordered per level of enrichment at Gujo-Hachiman. Ratios higher (lower) than 1.0 reflect enrichment (depletion) of a given element relative to Al.

dominant spectral peak from ~65 cm in unit I to ~16 cm in unit III (see Section 4.5), which documents a marked reduction in sedimentation rate upsection. The slightly greater (~6–8X) enrichment of TOC and strongly redox-sensitive metals (Mo, U, and V) in the black shale facies can be attributed primarily (50–70%) to a reduced biogenic silica flux and secondarily (30–50%) to other factors (e.g., enhanced sinking flux of organic matter, more reducing conditions). Relative to Gujo-Hachiman, the decrease in biogenic SiO_2 abundance from the chert facies (79%) to the black shale facies (57%) at Ubara corresponds to a smaller reduction (2.1X) in the sinking flux of this component, but one that is also almost exactly the inverse of the 2X enrichments observed for the detrital elements (Table 2). The chert-to-black shale ratios for TOC (4.0X) and the strongly redox-sensitive metals (~5–10X) at Ubara are larger than the ~2X change associated with biogenic SiO_2, indicating that ~20–50% of the increase in the fluxes of these components can be attributed to a reduced biogenic silica flux and ~50–80% to other factors.

4.3. C–S–Fe relationships

Proxies related to the C–S–Fe system show distinct patterns of covariation that potentially comment on environmental controls in each study section. Within the black shale facies, TOC exhibits a negative relationship to S at Gujo-Hachiman ($r = -0.62$, $n = 13$, $p(\alpha) < 0.05$) and a positive relationship to S at Ubara ($r = +0.44$, $n = 11$, $p(\alpha) < 0.05$; Fig. 6A). All samples from both sections (except for some chert samples from Gujo-Hachiman) plot well above the oxic–suboxic C–S trend of Berner and Raiswell (1983). S exhibits positive covariation with total Fe in the black shale facies of both sections, as well as in the chert facies of Ubara (but not Gujo-Hachiman); this relationship is strongest for the black shale facies at Gujo-Hachiman ($r = +0.81$, $n = 13$, $p(\alpha) < 0.01$; Fig. 6B). These patterns are consistent with derivation of much of the S and Fe in the study sections (except for the chert facies at Gujo-Hachiman) through the flux of syngenetic framboidal pyrite to the sediment, as well as with Fe limitation of pyrite formation (Berner and Raiswell, 1983; Raiswell and Berner, 1985).

DOP exhibits positive covariation with S in both study sections, although the relationship is markedly stronger for the black shale facies than for the chert facies in each section (e.g., at Gujo-Hachiman, $r = +0.56$, $n = 13$, $p(\alpha) < 0.05$; Fig. 6C). However, the chert and black shale facies exhibit markedly different DOP-S trends, with considerably higher S concentrations associated with a given DOP value in the black shale facies. The first observation implies a higher flux of framboidal pyrite to the sediment under more reducing conditions, although the second observation suggests that benthic redox conditions (as proxied by DOP) were not tightly coupled to the flux of framboidal pyrite (see Section 5.2). S concentrations generally vary negatively with $\delta^{34}S_{py}$, a relationship that is strongest for the black shale facies at Ubara ($r = -0.78$, $n = 11$, $p(\alpha) < 0.01$; Fig. 6D). The chert and black shale facies in each section exhibit markedly different trends for $\delta^{34}S_{py}$-[S], as shown by higher S concentrations for a given $\delta^{34}S_{py}$ value in the black shale facies. DOP does not appear to exhibit a systematic relationship to $\delta^{34}S_{py}$ within individual facies, although black shale samples tend to exhibit higher DOP and lower $\delta^{34}S_{py}$ values than chert samples (Fig. 6E). These patterns are consistent with increased fluxes of ^{34}S-depleted framboidal pyrite to the sediment under the more reducing conditions that existed during deposition of the black shale facies at each study locale.

4.4. MS–Fe relationships

The chert and black shales facies in the Gujo-Hachiman section exhibit relationships between MS values and Fe concentrations that may permit inferences regarding the identity of magnetic phases in the sediment. MS values exhibit a significant positive relationship to non-pyrite Fe in the chert facies ($r = +0.49$, $n = 86$, $p(\alpha) < 0.01$; Fig. 7A). Non-pyrite Fe is present mainly in paramagnetic clay minerals (yielding a low MS signal) as well as in small quantities of ferrimagnetic phases (yielding a high MS signal; Ellwood et al., 2000). The fact that non-pyrite Fe exhibits a weaker correlation with percent illite ($r = +0.26$; not shown) than with MS suggests that the MS signal derives mainly from non-clay detrital magnetic phases such as magnetite. MS values are on average about 0.5 log units greater for chert than for black shale samples of comparable Fe concentrations (Fig. 7A). This observation is consistent with a greater fraction of reactive Fe having been reduced and converted to pyrite in the black shale facies (cf. Fig. 5) and, hence, more of the remaining non-pyrite Fe being resident in weakly magnetic clay minerals rather than in ferrimagnetic phases. MS values show only a weak relationship to pyrite Fe in both facies (Fig. 7B), indicating that pyrite is not a major carrier of the MS signal. This inference is supported by the observation that relatively pure pyrite samples consistently yield MS values $<10^{-9}\ m^3\ kg^{-1}$ (Ellwood et al., 2000), well below most MS values reported for the study units (Fig. 4B).

4.5. Time series analysis

Both study sections exhibit pronounced lithologic cyclicity at a sub-meter scale. Cyclicity is best developed in the profiles for major lithologic components (Fig. 4A), MS (Fig. 4B), and Al (Fig. 4C), reflecting an alternation between chert-rich and clay-rich layers. Similar patterns of lithologic cyclicity have been shown to record Milankovitch-band climatic cyclicity in Jurassic and Cretaceous radiolarites of the Pacific (Molinie and Ogg, 1992; Ogg et al., 1992).

The dominant frequencies represented by this cyclicity were determined using multitaper method (MTM) spectral analysis. For the Gujo-Hachiman section, spectral analysis was undertaken on the detrended chert abundance record (Fig. 8A; cf. Algeo et al., 2010). A whole-section power spectrum exhibits a dominant peak at 65 cm and secondary peaks at 144, 40, 27, and 21 cm (Fig. 8B). An evolutionary power spectrum (Fig. 8C) confirms the positions and persistence of the main spectral peaks, and additionally shows that (1) the 65-cm peak undergoes repeated bifurcations up the section, possibly related to frequency modulations expected for the 100-kyr short-eccentricity cycle (Schlager, 2005, his figure 5.7); (2) frequencies >2 cycles/m are evident mainly within a high-resolution sampling interval in the middle of the study section (−3.3 to −5.3 m); and (3) a pronounced shift toward higher frequencies occurs at the transition from the chert to the black shale facies (0 m). Thinning of cycles from ~65 cm in the chert facies to ~16 cm in the overlying black shale facies (Fig. 8C) implies a ~4X decrease in sedimentation rates, a decrease that is consistent with sinking flux changes resulting from a sharp reduction in biogenic silica at the chert-black shale facies contact (see Section 5.1).

For the Ubara section, spectral analysis was undertaken on the detrended illite abundance record (Fig. 9A). A whole-section power spectrum exhibits a dominant peak at 45.5 cm and secondary peaks at 96.2, 22.7, and 15.6 cm (Fig. 9B). The 45.5-cm peak appears to be the most stable and is likely to represent the dominant cycle scale at Ubara. The 96.2-cm peak reflects a single "cycle" through the data series and cannot be interpreted as a true periodic signal. The 22.7-cm peak may be either a second-order harmonic of the 45.5-cm cycle or a higher-frequency fundamental cycle. The limited number of samples ($n = 25$) and their irregular spacing (5.4 ± 2.9 cm, but locally to 16 cm between adjacent samples) restricts the range of resolvable frequencies to wavelengths>~16.5 cm. The peak at 15.6 cm falls outside the range of resolvable frequencies; it may reflect a fundamental cyclicity at a shorter, but indeterminate, length scale in the Ubara section. The section is too short and undersampled to determine if any of these peaks exhibit a shift towards higher frequency upsection, as observed for Gujo-Hachiman (Fig. 8C).

The temporal significance of the spectral peaks in the two study sections can be inferred from several arguments. First, assignment of the 100-kyr short-eccentricity orbital cycle to the dominant 65-cm peak at Gujo-Hachiman yields an estimated duration for the section that is consonant with known biostratigraphic and geochronologic constraints. In this case, the 7.0-m-thick chert facies represents a depositional interval of ~1.1 Myr, i.e., within the range of permissible limits for the *N. optima* radiolarian zone, which corresponds to the latter half of the ~3-Myr-long Changxingian stage of the Upper Permian (Fig. 1B). The overlying 65-cm-thick black shale facies represents a depositional interval of ~400 kyr (reflecting a 4X decrease in the black shale facies, as discussed above), i.e., within the range of permissible limits for the ~0.7-Myr-long Griesbachian substage of the Lower Triassic (Fig. 1B). Second, the durations above yield average sedimentation rates of 7–8 m Myr^{-1} for the chert facies and ~2 m Myr^{-1} for the black shale facies. Such slow accumulation rates are consistent with sedimentation in an abyssal setting (Molinie and Ogg, 1992; Ogg et al., 1992; Olivarez-Lyle and Lyle, 2006). Assignment of the 406-kyr long-eccentricity orbital periodicity to the 65-cm peak would yield durations that exceed permissible limits for the Changxingian and Griesbachian. Although shorter periodicities cannot be entirely excluded, they also seem unlikely: (1) the ~41-kyr obliquity periodicity is generally not strongly expressed in low-latitude marine systems, and (2) if the 65-cm peak represented forcing by the 19- to 23-kyr precession periodicity, then the amount of time represented by the chert facies would be reduced to ~200 kyr, which is rather too short for a stratigraphic interval corresponding to more than half of the Changxingian stage. Thus, the 65-cm peak of the Gujo-Hachiman section is most likely to represent forcing by the 100-kyr short-eccentricity orbital cycle; analogous arguments can be applied to link the dominant 45-cm cycle in the Ubara section to the same orbital cycle. Recognition of orbital periodicities in the study section holds potential for development of a "floating" astronomical time scale across the PTB that would assist ultra-high-resolution interregional correlation for sections of this age (Hinnov, 2000).

4.6. Depth–age models and flux calculations

The chemostratigraphic and spectral data above provide a basis for generating depth–age models and calculating sediment fluxes for the study sections. We constructed two depth–age models based on slightly different premises. Both models depend on the observation that chert is the largest single component of the study units (Fig. 4A),

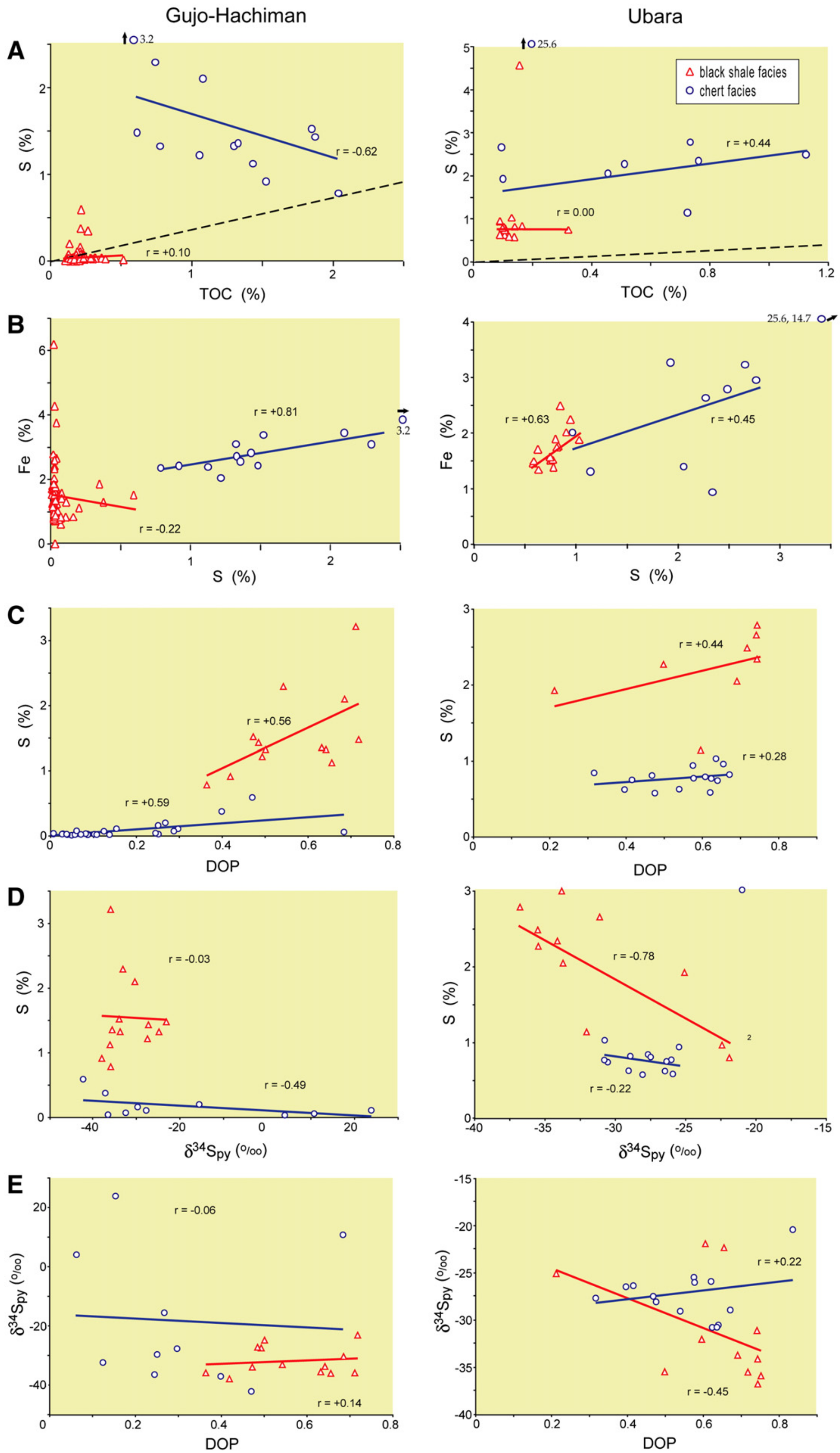
Gujo-Hachiman
Ubara
A
B
C
D
E
black shale facies
chert facies
S (%)
TOC (%)
Fe (%)
DOP
δ34Spy (‰)
3.2
25.6
25.6, 14.7
r = -0.62
r = +0.10
r = +0.44
r = 0.00
r = +0.81
r = -0.22
r = +0.63
r = +0.45
r = +0.56
r = +0.59
r = +0.44
r = +0.28
r = -0.03
r = -0.49
r = -0.78
r = -0.22
r = -0.06
r = +0.14
r = +0.22
r = -0.45

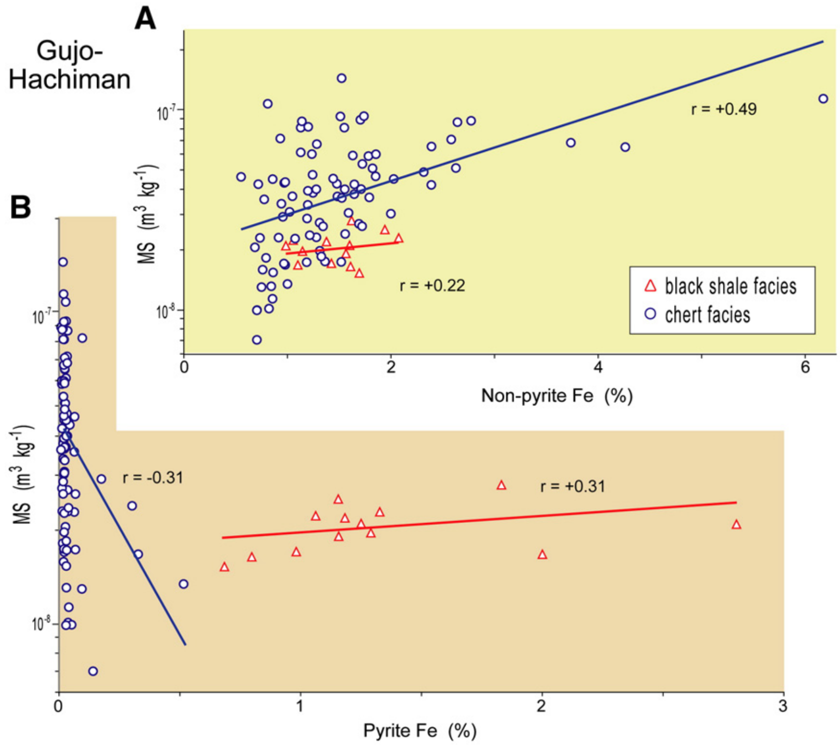

Fig. 7. MS crossplots: (A) non-pyrite Fe vs. MS, and (B) pyrite Fe vs. MS. Pyrite Fe and non-pyrite Fe concentrations were calculated per Eqs. (3) and (4).

and the inference that variation in other sediment components between the chert and black shale facies can be accounted for largely through changes in the sinking flux of biogenic silica (see Sections 4.2 and 5.1). Model 1 uses the raw percent chert curve for each section (Fig. 10A, solid line) to calculate linear sedimentation rates (Fig. 10B, solid line), based on the premise that all changes in the latter parameter were due to variation in biogenic silica fluxes:

$$LSR_i^{i+1} = k \times 100 / (100 - \%\mathrm{Chert}) \tag{5}$$

where LSR = linear sedimentation rate for the stratigraphic interval between successive samples i and i + 1, and k is a relational constant with units of m Myr^{-1} that was adjusted to match the temporal constraints discussed below. Model 2 substitutes the smoothed percent chert curve (Fig. 10A, dashed line) into Eq. (5) to calculate linear sedimentation rates (Fig. 10B, dashed line) for each section, based on the premise that only first-order (low-frequency) changes in the latter parameter were controlled by biogenic silica fluxes and that second-order (high-frequency) changes were due to variation in the fluxes of other sediment components.

The spectral analytical results from Section 4.5 provide the basis for constraining time in the two study sections. For Gujo-Hachiman, the lowermost 4.7 m of the chert facies exhibits a nearly invariant dominant spectral peak at ~1.6 cycles per meter (Fig. 8), implying little or no secular variation in sedimentation rates. If this peak represents the ~100-kyr short-eccentricity orbital cycle, then the basal 4.7 m of the chert facies was deposited in 0.75 Myr at an average sedimentation rate of 6.25 m Myr^{-1} (Fig. 10B–C). For Ubara, which is too short a section to permit an evolutionary spectral analysis, the duration of the full (134 cm) thickness of the section was estimated on the basis of the dominant 45.5-cm spectral peak (Fig. 9) representing the ~100-kyr short-eccentricity orbital cycle. This calculation yielded an estimated duration of ~0.30 Myr at an average sedimentation rate of 4.54 m Myr^{-1} (Fig. 10B-C). Per these temporal constraints, the relational constant (k) for each depth–age model was adjusted to satisfy the equation:

$$\int_b^t d_i^{i+1} / LSR_i^{i+1} = \tau. \tag{6}$$

This equation integrates time as a function of the vertical distance (d) and linear sedimentation rate (LSR) between successive samples i and i + 1 from the base (b) to the top (t) of the stratigraphic interval of interest (i.e., −7.0 to −2.3 m at Gujo-Hachiman, and −1.10 to 0.24 m at Ubara), where τ is the duration of the stratigraphic interval of interest (i.e., 0.75 Myr at Gujo-Hachiman and 0.30 Myr at Ubara).

The two depth–age models yield similar first-order trends but differing degrees of high-frequency variation in sedimentation rates for the two study sections (Fig. 10B). Model 1 exhibits strong short-term variation in sedimentation rates as a function of the high-frequency variation of its input variable (i.e., raw chert abundance; Fig. 10A), whereas model 2 exhibits no short-term variation in sedimentation rates as a function of the lack of high-frequency variation in its input variable (i.e., smoothed chert abundance; Fig. 10A). However, the high-frequency variation in sedimentation rates that characterizes model 1 is averaged out at intermediate timescales, resulting in rather similar depth–age curves for both models (Fig. 10C). Depth–age models for Gujo-Hachiman show a sharp (~4X) decrease in sedimentation rates from unit I to unit III, whereas depth–age models for Ubara show a more modest (~2X) decrease from units I–II to unit III.

Fig. 6. C–S–Fe system crossplots for Gujo-Hachiman (left) and Ubara (right): (A) TOC vs. S, (B) S vs. Fe, (C) S vs. DOP, (D) S vs. $\delta^{34}S_{py}$, and (E) $\delta^{34}S_{py}$ vs. DOP. Dashed line in A is TOC-S trend for oxic marine facies from Berner and Raiswell (1983). For all plots, chert facies are shown as open circles and siliceous mudstone facies as filled triangles; note that units I and II correspond to the chert facies and unit III (and part of unit II at Ubara) to the siliceous mudstone facies. Note differences between the two lithofacies in all crossplots.

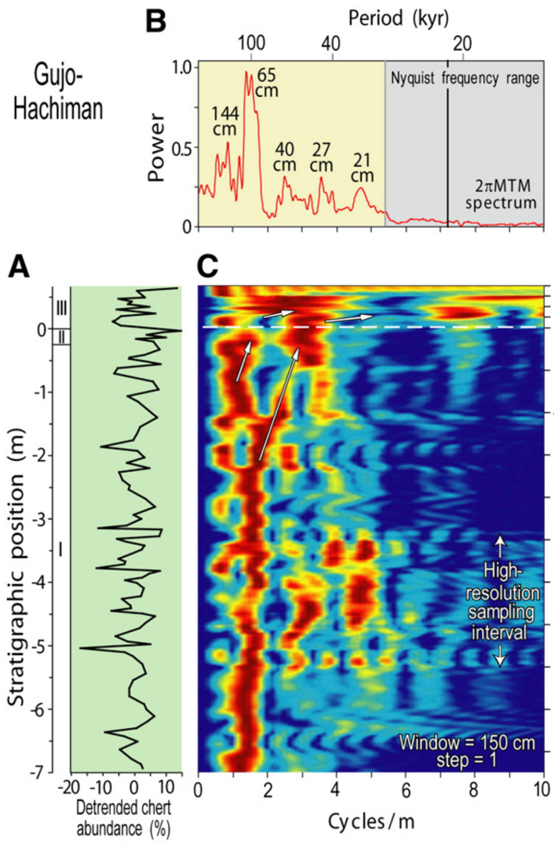

Fig. 8. Spectral analysis of Gujo-Hachiman section: (A) Detrended chert abundance (25% weighted-average LOWESS curve subtracted from %chert in Fig. 3A; data interpolated from an uneven sample spacing of 7.7 ± 3.8 cm to an even spacing of 1 cm); (B) 2π multitaper spectrum for the whole section; and (C) evolutionary spectrogram using a 150-cm window, based on magnitude-squared Fourier transforms. The higher-frequency components at 21, 27, and 40 cm may represent precession and obliquity signals that are marginally resolved within this interval of more closely spaced samples (−3.3 to −5.3 m in the section). The lower frequency components at 65 cm and 144 cm comprise a modulation, evident in the evolutionary spectrogram, that may be related to the short (~100 kyr) eccentricity signal. There is a general shift toward higher frequencies across the contact between the underlying chert and overlying black shale facies (white arrows).

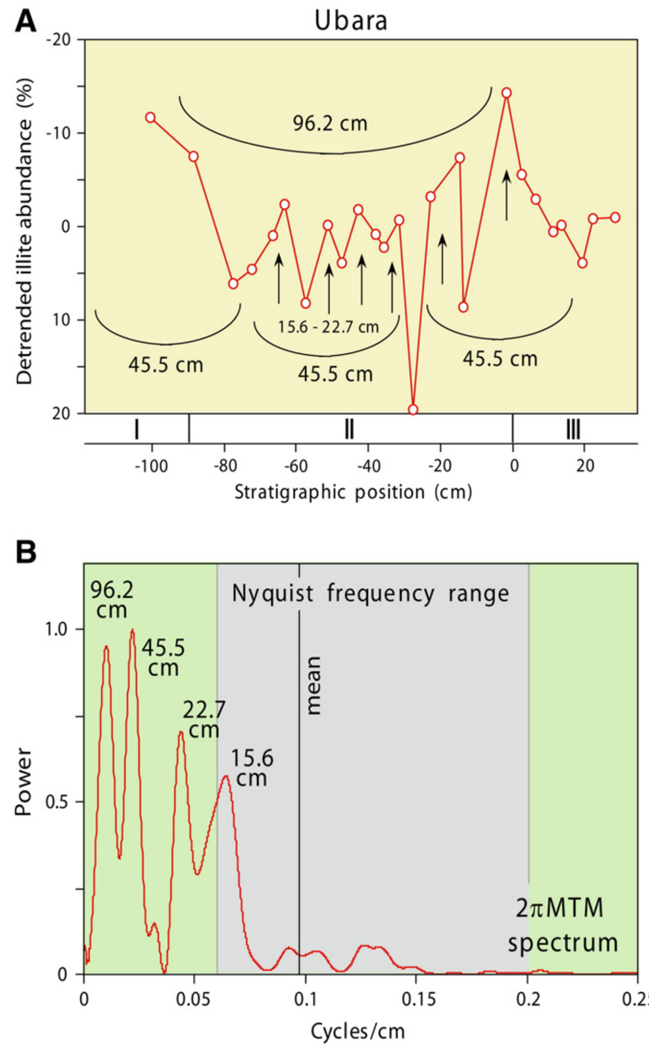

Fig. 9. Spectral analysis of Ubara section: (A) Detrended illite abundance (25% weighted-average LOWESS curve subtracted from %illite in Fig. 3A; data interpolated from an uneven sample spacing of 5.4 ± 2.9 cm to an even spacing of 1 cm); and (B) 2π MTM power spectrum of %illite series with peaks identified in terms of wavelength and Nyquist frequency range shown. The principal wavelengths identified in B are also shown in A.

Using the depth–age models calculated above, the fluxes (or accumulation rates) of individual sediment components to each study section were calculated as follows:

$$f(A)_i^{i+1} = [A]_i^{i+1} \times LSR_i^{i+1} \times \rho \tag{7}$$

where f(A) is the flux of component A in g cm^{-2} kyr^{-1}, [A] is the concentration of component A in weight percent, LSR is the linear sedimentation rate converted to cm kyr^{-1} for the stratigraphic interval i to i + 1, and ρ is sediment density in g cm^{-3} (for which a constant value of 2.5 was assumed). Because the same input parameter (either raw or smoothed chert concentrations; Fig. 10A) was used to calculate both sedimentation rates (Fig. 10B) and chert fluxes (Fig. 11A), these parameters necessarily exhibit identical patterns of stratigraphic variation. Model 1, which assumes that all variation in sedimentation rates is controlled by fluctuations in biogenic silica fluxes, yields considerably greater high-frequency variation in chert fluxes than model 2.

The component flux calculations yielded some intriguing results. Chert fluxes in both sections decline from values of ~1–2 g cm^{-2} kyr^{-1} in the chert facies to values <0.5 g cm^{-2} kyr^{-1} in the black shale facies (Fig. 11A). Illite fluxes are rather uniform through each section but are systematically higher at Ubara (~0.2–0.3 g cm^{-2} kyr^{-1}) relative to Gujo-Hachiman (~0.10–0.12 g cm^{-2} kyr^{-1}; Fig. 11B). TOC fluxes are low (mostly <5 mg cm^{-2} kyr^{-1}) through both sections (Fig. 11C). Pyrite fluxes are low (mostly <2 mg cm^{-2} kyr^{-1}) in the basal 5 m of the chert facies at Gujo-Hachiman but rise sharply (to 10–20 mg cm^{-2} kyr^{-1}) in the uppermost 1.5 m of the chert facies as well as in the overlying black shale facies (Fig. 11D). Ubara shows systematically higher pyrite fluxes (10–20 mg cm^{-2} kyr^{-1}) than Gujo-Hachiman, with two episodes in which pyrite fluxes peaked at >50 mg cm^{-2} kyr^{-1} (Fig. 11D).

With regard to secular variation in major component fluxes, the two depth–age models have somewhat different implications for the Gujo-Hachiman section. Model 1 shows strong dm-scale variation (i.e., at length scales associated with the dominant 65-cm spectral peak) in the fluxes of chert, TOC, and pyrite and relatively little variation in illite, whereas model 2 shows strong dm-scale variation in illite and lesser variation in the other component fluxes (Fig. 11). These observations might be taken as implicit validation of model 2 based on the argument (a version of Occam's razor) that variation in one proxy (illite) is more likely than concurrent variations in three proxies (chert, TOC, and pyrite). Secular variation in illite fluxes at orbital periodicities may have been due to climatically controlled fluctuations in weathering rates and/or wind shear that influenced the production and delivery of fine siliciclastic material to the study site.

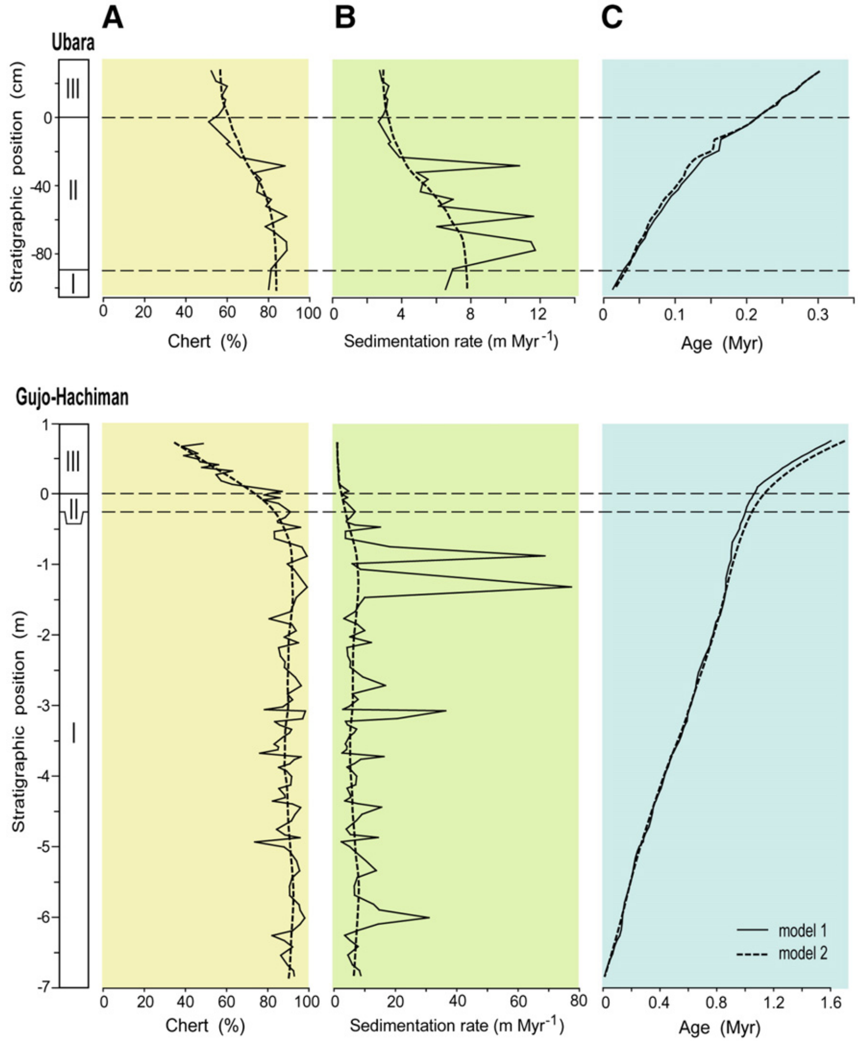

Fig. 10. Depth–age models for Gujo-Hachiman (below) and Ubara (above): (A) percent chert (input function), (B) linear sedimentation rate, and (C) depth–age model (calculated per Eqs. (5) and (6)). Model 1 is based on raw percent chert (solid lines), whereas model 2 is based on the smoothed first-order chert record (dashed lines).

However, the concurrent variations in fluxes yielded by model 1 may not be inherently improbable if, for example, chert and TOC were controlled by primary productivity, and pyrite covaried with them owing to coupling of water-column redox conditions to organic C export fluxes. Thus, it remains uncertain whether model 1 or model 2 is a more accurate representation of variation in sedimentation rates and major component fluxes in the two study sections.

5. Discussion

5.1. Major component fluxes

Biogenic silica fluxes to the sediment show substantial variability in the modern Pacific Ocean. Fluxes are mostly ~0.1 g cm^{-2} kyr^{-1} in high-nutrient low-chlorophyll (HNLC) regions of the tropical Pacific (Berelson et al., 1997; Blain et al., 1997), which is the same as the global average flux (Tréguer et al., 1995), but peak at ~0.25 g cm^{-2} kyr^{-1} near the equator (Murray and Leinen, 1993). However, higher fluxes (~0.5 to 2.0 g cm^{-2} kyr^{-1}) characterize high-productivity regions of the modern eastern Pacific and Southern oceans (Pondaven et al., 2000; Kienast et al., 2006) as well as parts of the Cretaceous equatorial Pacific (Thiede and Rea, 1981; Ogg et al., 1992). Diatoms are generally the largest contributor to the biogenic silica fraction, and very high fluxes (30–600 g cm^{-2} kyr^{-1}) are associated with local areas of diatom blooms in the modern ocean (Kemp et al., 2006; Xiong et al., submitted for publication). Radiolarian silica fluxes tend to be lower, as shown by equatorial Pacific radiolarites of Jurassic to early Tertiary age (mostly 1–3 g cm^{-2} kyr^{-1}, but locally to ~10 g cm^{-2} kyr^{-1}; Karl et al., 1992). Radiolarian fluxes in the modern equatorial Pacific are substantial and closely tied to climate-driven productivity cycles (Okazaki et al., 2008). Biogenic silica accumulation rates are dependent on preservation efficiencies: typically 1 to 6% (global average ~2.5%) of biogenic silica production is preserved in the sediment, with higher preservation efficiencies associated with higher production and accumulation rates (Pondaven et al., 2000). In the context of these data, the biogenic silica fluxes in the chert facies of the two study sections (~1–2 g cm^{-2} kyr^{-1}; Fig. 11A) are indicative of moderate to high-productivity settings. Biogenic silica fluxes were lower in the black shale facies (<0.5 g cm^{-2} kyr^{-1}), but this reduction is likely to have been a consequence of radiolarian extinctions during the PTB crisis rather than to a decline in marine primary productivity during the Early Triassic (see Section 5.3).

The flux of siliciclastic material, mostly through eolian transport, to the modern mid-Pacific Ocean is generally low (<0.1 g cm^{-2} kyr^{-1}; Murray and Leinen, 1993; McGee et al., 2007), and similar fluxes have prevailed since 90 Ma (Rea and Janacek, 1981). Higher values (to ~2.5 g cm^{-2} kyr^{-1}) are associated with elevated rates of volcanogenic input, as on the Pleistocene Shatsky Rise (Gylesjö, 2005) and in the mid-Pacific during the mid-Cretaceous interval of heightened plume activity (Rea and Janacek, 1981). In contrast, fluxes of siliciclastic

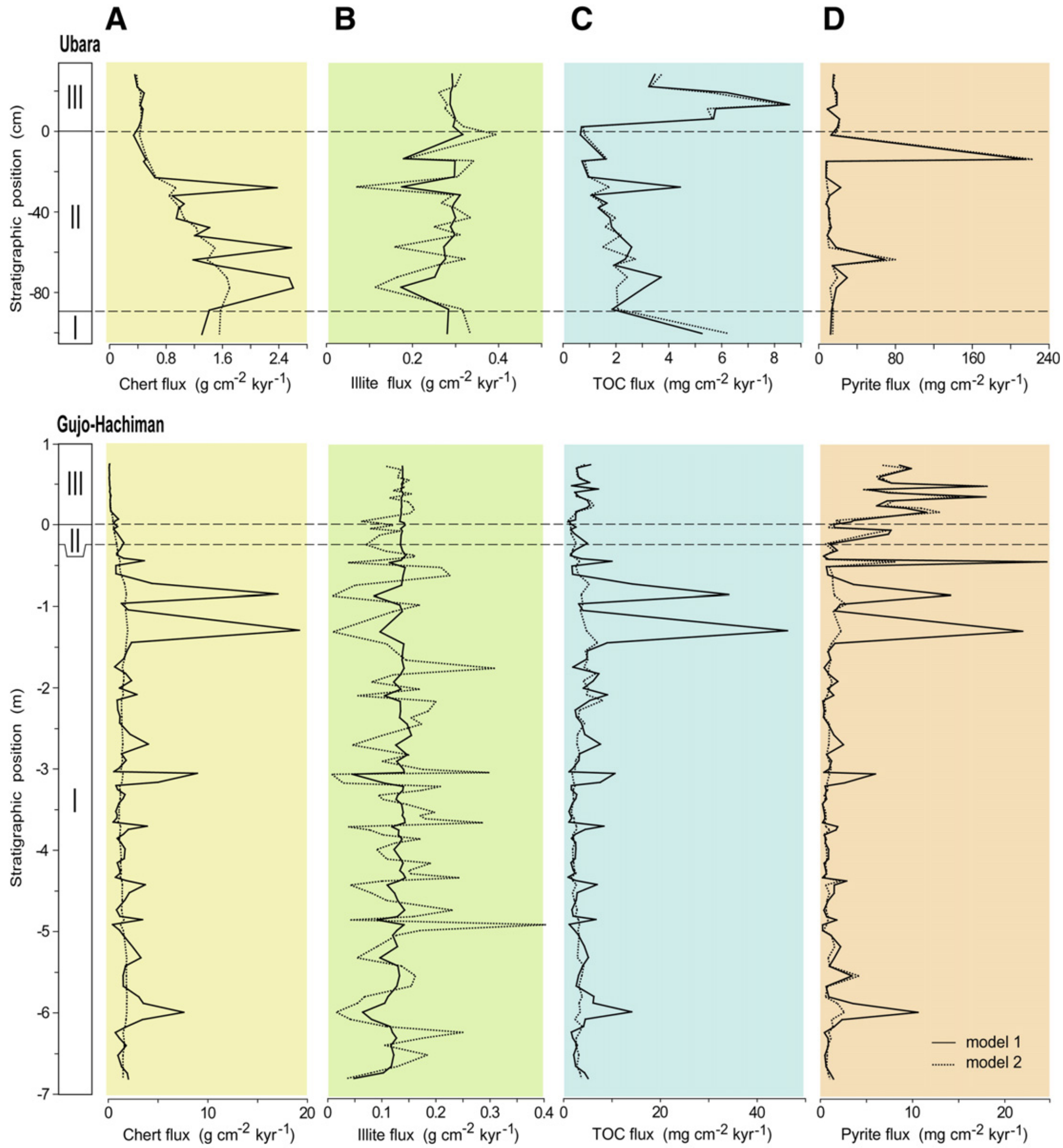

Fig. 11. Fluxes of major sediment components to the sediment for Gujo-Hachiman (below) and Ubara (above): (A) chert flux, (B) illite flux, (C) TOC flux, and (D) pyrite flux (calculated per Eq. (7)). Fluxes are given in units of grams per square centimeter per thousand years; models 1 and 2 refer to depth–age models of Fig. 10.

detritus to continent-margin settings can be much higher, e.g., ~75–150 g cm^{-2} kyr^{-1} on the Peru Shelf (Böning et al., 2004). The low fluxes of illite in the two study sections (~0.2–0.3 g cm^{-2} kyr^{-1} at Ubara, and ~0.10–0.12 g cm^{-2} kyr^{-1} at Gujo-Hachiman; Fig. 11B) are consistent with a mid-ocean location for these sections. The systematically higher fluxes at Ubara may indicate greater proximity to volcanic or continental sources of siliciclastics, or location of the Ubara section within a zone of elevated eolian transport, relative to the Gujo-Hachiman section (Fig. 12).

TOC fluxes to the sediment exhibit strong spatial variability in marine systems. The modern equatorial Pacific shows fluxes of ~2–6 mg cm^{-2} kyr^{-1} (Murray and Leinen, 1993), similar to values during the Eocene (Olivarez-Lyle and Lyle, 2006) but lower than typical values during the Cretaceous (10–30 mg cm^{-2} kyr^{-1}, but locally to ~100–900 mg cm^{-2} kyr^{-1}; Thiede and Rea, 1981). Regions of the modern ocean are also characterized by much higher TOC fluxes, e.g., 1–10 g cm^{-2} kyr^{-1} in high-productivity zones of the Southern Ocean (Pondaven et al., 2000) and 10–50 g cm^{-2} kyr^{-1} in high-productivity upwelling systems such as the Peru Shelf (Böning et al., 2004). Calculated TOC fluxes for the two study units (mostly <5 mg cm^{-2} kyr^{-1}; Fig. 11C) are low in part due to loss of organic carbon through thermal maturation of the sediment during low-grade regional metamorphism (Isozaki, 1997a; Nakajima, 1997). Reconstruction of original (i.e., depositional) TOC concentrations is necessarily speculative, but Raiswell and Berner (1987) showed that TOC values decrease by roughly a factor of four as vitrinite reflectance (R_0) values increase from 0 to 2.0 (equivalent to burial temperatures of ~200 °C). Based on this relationship, C export fluxes to the study sites were probably originally in the range of 10–20 mg cm^{-2} kyr^{-1}. In the context of the modern data above, these values suggest that the study sites were located in a region of moderate to high primary productivity. The observation that TOC fluxes are stable or increase across the chert-to-black shale facies contact in both study sections (Fig. 11C) implies that primary productivity rates in the mid-Panthalassic Ocean probably did not decrease as a result of the PTB crisis.

Pyrite burial fluxes are low in oxic to suboxic settings of the modern deep ocean (Berner, 1972; Dale et al., 2009). In anoxic settings, pyrite burial fluxes can vary considerably. The modern Black

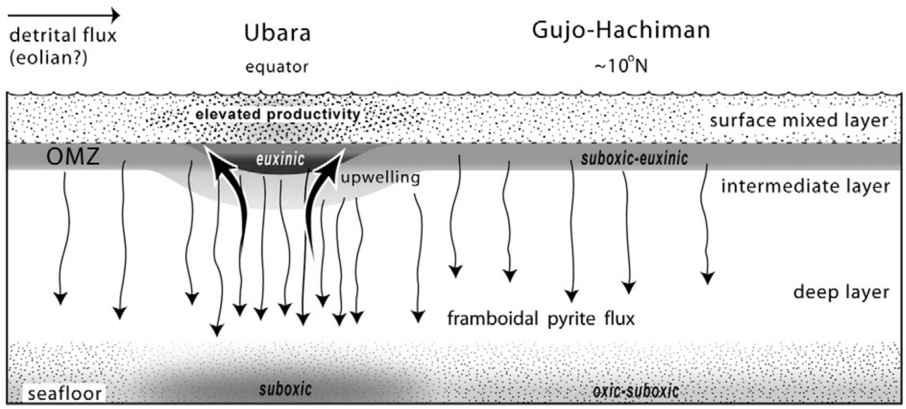

Fig. 12. Inferred paleoceanographic settings of Gujo-Hachiman and Ubara sections. Ubara was located within the zone of equatorial divergent upwelling and closer to the source of the detrital (eolian?) fraction; Gujo-Hachiman was located peripheral to the zone of equatorial upwelling and further from the source of the detrital fraction. At both locales, intensification of anoxia during the latest Permian and Early Triassic was greatest within the oxygen-minimum zone (OMZ) rather than at the seafloor.

Sea has a flux of ~1–2 g cm^{-2} kyr^{-1} to the sediment, of which ~80–95% represents syngenetic framboidal pyrite (calculated using data in Wilkin and Arthur, 2001). Pyrite burial fluxes can be even higher in high-productivity upwelling systems such as the Peru Shelf (~2–10 g cm^{-2} kyr^{-1}; Böning et al., 2004; n.b., S fluxes converted to pyrite equivalent). In this context, pyrite fluxes are low in the black shale facies of the two study units (mostly 10–20 mg cm^{-2} kyr^{-1} with local peaks to >50 mg cm^{-2} kyr^{-1}) and very low in the chert facies at Gujo-Hachiman (<2 mg cm^{-2} kyr^{-1}; Fig. 11D). There is no reason to suppose the loss of pyrite S through thermal maturation of the study sections (n.b., petrographic data indicate that both framboids and euhedral grains remain well-preserved), so a more likely explanation is that pyrite formation was strongly Fe-limited owing to the location of the study sites in the central Panthalassic Ocean, far from terrestrial sources of detrital Fe (Fig. 1C).

5.2. Redox conditions

Several geochemical proxies may comment on benthic redox conditions at the study sites, the foremost being degree-of-pyritization (DOP). Raiswell et al. (1988) originally defined DOP in relation to three redox facies: (i) an aerobic facies, characterized by an abundant benthic biota and strongly bioturbated sediment (DOP < 0.45), (ii) a restricted facies, characterized by a limited benthic biota and weakly bioturbated sediment (DOP >0.45 and <0.75), and (iii) an inhospitable facies, characterized by a lack of benthic biota and laminated sediment (DOP >0.75). Based on this spectrum, the study units show considerable variation in redox conditions. At Gujo-Hachiman, DOP values are mostly <0.2 in the chert facies, suggesting oxidizing conditions, and rise to 0.40–0.65 in the black shale facies (Fig. 4D), suggesting restricted (i.e., suboxic) rather than inhospitable (i.e., anoxic) conditions. At Ubara, DOP values are mostly between 0.40 and 0.75 (with only limited differences between facies; Fig. 4D), suggesting redox variation in the range of restricted (suboxic) to slightly inhospitable (weakly anoxic) conditions for this section.

Redox-sensitive trace metals such as Mo, U, and V show low concentrations (that are consistent with background detrital values) in the chert facies of both units (Fig. 4F), showing no evidence of authigenic enrichment as is common in marine systems with anoxic bottom waters (e.g., Algeo and Tribovillard, 2009). Although the black shale facies of both study sections exhibits a sharp increase in raw concentrations of these trace metals, the actual increase in their flux to the sediment (when corrected for biogenic silica dilution; Table 2, see Section 4.2) is rather small, <2X at Gujo-Hachiman and 2–5X at Ubara. The greater increase in the flux of these trace metals at Ubara is consistent with the higher DOP values exhibited by that section for both the chert and black shale facies, relative to the corresponding facies at Gujo-Hachiman. Based on these considerations, it appears that redox conditions were persistently somewhat more reducing at Ubara than at Gujo-Hachiman, and that this difference persisted across through the chert-to-black shale facies transition. In summary, these results suggest that Panthalassic deepwaters were oxic to suboxic during deposition of Late Permian chert facies and suboxic to weakly anoxic during deposition of latest Permian to Early Triassic black shale facies (Fig. 12). Given the consistency of redox interpretations yielded by the DOP and trace-metal data, these results may be considered a reliable record of benthic redox patterns at the study sites.

The conclusions above are at odds with some earlier interpretations of redox conditions in the deep Panthalassic Ocean. The lithologic transition from red cherts to gray cherts to black shales in Japanese PTB sections has been cited as evidence of a progressive shift from oxic to suboxic and then to euxinic conditions (Isozaki, 1994, 1997b; Suzuki et al., 1998). Various lines of evidence in support of benthic anoxia have been offered: (1) Mössbauer spectroscopic data show that Fe is more than 50% reduced in the gray cherts and mostly (75–100%) reduced in the black shales (Matsuo et al., 2003), and (2) Mn concentrations decrease to near zero and Ce/Ce* ratios increased to ~1.0 at the red chert-to-gray chert transition near the Guadalupian/Lopingian (Middle/Upper Permian) boundary (Kato et al., 2002). However, other lines of evidence suggest less-than-fully anoxic conditions during deposition of Japanese PTB sections: biofabric studies have shown that Upper Permian gray cherts are extensively bioturbated, and that uppermost-Changxingian to Lower Triassic black shales locally show some evidence of a burrowing infauna (Kakuwa, 1996, 2008). The juxtaposition of bioturbation with geochemical evidence of oxygen-depleted conditions may record temporally fluctuating redox conditions (cf. Kenig et al., 2004), although the geochemical evidence cited above is also consistent with predominantly suboxic conditions during black shale deposition.

One line of evidence from the study sections unambiguously supports inferences of water-column anoxia: the presence of syngenetic pyrite framboids (Fig. 3). Pyrite framboids are spherical aggregates of submicron-sized crystals with a raspberry-like appearance that form via the reaction of H_2S with iron particles through mono-sulfide intermediates (Wilkin et al., 1996). Syngenetic framboids (i.e., those formed in an euxinic water column) are generally limited to a maximum diameter of ~5–7 μm in consequence of the rapid settling of larger particles from suspension. Where present, framboids often dominate the pyrite fraction (comprising 80–95% of pyrite in units I and II of the Black Sea) and exhibit strongly ^{34}S-depleted compositions owing to near-maximum fractionation during bacterial sulfate reduction within a sulfate-unlimited reservoir ($\Delta^{34}S^{SO_4^{2-}}_{FeS_2} = 55-60‰$ for the Black Sea; Wilkin and Arthur, 2001).

The abundance and isotopic composition of framboidal pyrite in unit III of Gujo-Hachiman and units II and III of Ubara provide evidence of at least intermittently euxinic conditions at the study sites. Framboidal pyrite comprises 3–8% (by volume) of the black shale facies of each study section (Fig. 3) and has $\delta^{34}S_{py}$ compositions that are markedly depleted relative to the chert facies (Fig. 4H). An increase in framboidal pyrite accompanied by a shift toward more ^{34}S-depleted values, typically to between −30 and −40‰ CDT (as in the present study) has been reported for other PTB sections in Japan (Ishiga et al., 1993; Kajiwara et al., 1994) and elsewhere (Nielson and Shen, 2004; Algeo et al., 2008). An average $\delta^{34}S_{py}$ for the black shale facies of both of the present study sections (~−31±6‰) represents a $\Delta^{34}S_{FeS_2}{}^{SO_4^{2-}}$ of ~41 to 43‰ relative to a latest Permian seawater sulfate value of +10 to +12‰ (Strauss, 1997), consistent with maximum fractionation in a sulfate-unlimited system such as the open ocean.

Because the DOP and trace-metal proxies discussed above imply oxic–suboxic to at most weakly anoxic conditions in Panthalassic deepwaters during the Late Permian to Early Triassic, the redox evidence provided by ^{34}S-depleted framboidal pyrite in the study sections is probably an indication of the development of euxinia higher in the water column (Fig. 12). In the modern Pacific Ocean, an oxygen-minimum zone (OMZ) exists just below the surface mixed layer as a result of the strong export flux of organic C in combination with reduced ventilation (Tomczak and Godfrey, 2005). The OMZ is usually most intense at depths of ~500–1000 m but rises to shallower depths (<200 m) across extensive areas of the eastern tropical Pacific, in which C export fluxes are greater and ventilation more reduced than elsewhere (Levitus and Boyer, 1994). Expansion of the tropical Panthalassic OMZ during the latest Permian–Early Triassic was probably due to a combination of factors, including climatic warming (reducing the solubility of dissolved oxygen in seawater; Wignall, 2007), lowered atmospheric pO_2 (Huey and Ward, 2005), and enhanced marine primary productivity (as inferred from paleoproductivity proxies in the present study; see Section 5.3). Enhanced marine productivity may have been driven by elevated rates of chemical weathering of land areas during the Early Triassic (Sheldon, 2006; Algeo and Twitchett, in press). An expanded, at least intermittently sulfidic OMZ in the Permo-Triassic Panthalassic Ocean would have provided a source for toxic H_2S-bearing waters that episodically upwelled onto shallow continental shelves and platforms (Grice et al., 2005; Algeo et al., 2008; Cao et al., 2009). Intensification of the OMZ is also projected to be a consequence of modern climatic warming (Schaffer et al., 2009), making analysis of Permo-Triassic oceanic conditions relevant to discussions of present-day oceanographic changes.

The considerations above strongly counter hypotheses proposing widespread development of anoxia in the Permian–Triassic deep ocean (Isozaki, 1994; Wignall and Twitchett, 1996; Isozaki, 1997b; Wignall and Twitchett, 2002). Such hypotheses have been challenged previously on the basis of paleoceanographic modeling results, which are unable to achieve prolonged stagnation of global ocean circulation (Hotinski et al., 2001). Reduced dissolved oxygen levels in Permian–Triassic seawater have been linked instead to changes in sea-surface temperatures, freshwater fluxes, nutrient levels, and particle penetration depths (Hotinski et al., 2001; Kiehl and Shields, 2005; Winguth and Maier-Reimer, 2005), and model results suggest that low-oxygen conditions expanded most dramatically within the OMZ rather than at abyssal depths. The results of the present study are consistent with these results and may contribute to a resolution of existing model-data discrepancies on this issue. Further, the 10- to 20-Myr-long interval of reduced oxygen levels ("superanoxia") in the Panthalassic Ocean proposed by Isozaki (1994, 1997b) appears unviable in view of recently published geochronological studies shortening the duration of the Early Triassic to a few million years (Mundil et al., 2010). Although some shift in oceanic redox conditions may have occurred as early as the Guadalupian–Lopingian boundary (Kato et al., 2002), persistently suboxic to anoxic conditions existed only during the interval from the latest Changxingian to approximately the Smithian–Spathian substage boundary of the Early Triassic (Kakuwa, 1996), an interval of no more than ~2 Myr duration (Mundil et al., 2010).

5.3. Biotic productivity

Changes in marine primary productivity and the composition of planktic communities may have played important roles in the PTB crisis. Estimated organic carbon sinking fluxes in the range of 10–20 mg cm^{-2} kyr^{-1} imply moderate to high primary productivity at both study sites (see Section 5.1), with no decline (and possibly an increase) in productivity rates from the Late Permian to the Early Triassic (Fig. 11). Given large uncertainties in paleoproductivity estimates based on TOC data, it is useful to evaluate other productivity proxies such as excess Ba (Ba_{xs}) and P. Ba_{xs} is the amount of Ba in the sediment in excess of the estimated detrital Ba fraction:

$$Ba_{xs} = Ba_{sample} - Ba_{PAAS} * Al_{sample} / Al_{PAAS} \tag{8}$$

where PAAS is a shale standard based on the composition of Post-Archean Australian Shales (Taylor and McLennan, 1985). Excess Ba develops as barite is precipitated on the surfaces of decaying organic particles in the water column, where high concentrations of reoxidized H_2S encounter Ba in seawater (Dehairs et al., 1992). Ba_{xs} concentrations are commonly elevated (~1000–5000 ppm) in high-productivity regions of the modern equatorial Pacific (Murray and Leinen, 1993). The study units yield mostly low to moderate estimates of Ba_{xs}, 470±180 ppm at Gujo-Hachiman (with no significant difference between facies) and 375±75 ppm for the chert facies at Ubara. However, several samples from the black shale facies at Ubara yield Ba_{xs} concentrations between 2000 and 9000 ppm. Although further investigation is needed in order to determine the frequency and extent of such Ba_{xs} anomalies, the available data can be interpreted as evidence of (at least episodic) increases in productivity in the Early Triassic Panthalassic Ocean. Interpretation of Ba_{xs} as a paleoproductivity proxy is potentially complicated by influences on excess Ba retention: (i) low concentrations of seawater sulfate, as inferred for the Late Permian–Early Triassic (Bottrell and Newton, 2006), reduce the solubility product for barite in seawater, and (ii) anoxic conditions in sediment porewaters cause reductive dissolution of sedimented barite. The significance of these factors for Ba_{xs} accumulation in the study units is uncertain, although if benthic redox conditions were predominantly suboxic (see Section 5.2) then sedimented Ba_{xs} may have been largely preserved. Ba_{xs} concentrations in the study sections are not sufficiently high to suggest a predominantly hydrothermal source (McManus et al., 1998).

A second geochemical proxy for paleoproductivity is phosphorus (P). P is transferred to the sediment mainly as organically bound P, most of which is subsequently liberated through remineralization of organic matter; long-term retention of P in the sediment requires adsorption onto FeOOH phases and subsequent precipitation of authigenic phosphate minerals (Algeo and Ingall, 2007). P/Ti ratios average 0.17±0.23 for both facies at Gujo-Hachiman (with a few samples yielding values as high as 1.3) and 0.34±0.55 for the chert facies at Ubara. These ratios are close to those for PAAS (0.13) and average pelagic clay (0.33) and far below those (~2–8) associated with regions of elevated productivity in the modern equatorial Pacific (Murray and Leinen, 1993). However, the black shale facies at Ubara exhibits higher P/Ti ratios (average 0.79±1.63) with some samples yielding values as high as 5.5. Such values imply elevated levels of primary productivity in Early Triassic Panthalassic Ocean surface waters, consistent with inferences based on Ba_{xs} data (see above). Use of P as a paleoproductivity proxy is potentially complicated by influences on P retention in the sediment: (i) porewater redox conditions (n.b., oxic to suboxic conditions promote retention), and

(ii) the availability of Fe compounds for adsorption of P (Algeo and Ingall, 2007). The largely suboxic bottomwaters inferred for the two study sites (Fig. 12) probably favored the retention of P liberated from organic matter, but low mineral Fe concentrations (owing to a limited detrital flux; see Section 5.1) may have limited the retention of organic P.

The composition of the ocean plankton community was markedly altered during the PTB crisis. For example, biomarker studies have demonstrated a shift toward greater abundances of green sulfur and N-fixing diazotrophic bacteria among primary producers in the Tethyan region (Grice et al., 2005; Xie et al., 2007; Cao et al., 2009). Although biomarker analysis of Japanese PTB sections may prove difficult or impossible owing to high thermal maturity, their microfossil records allow some inferences concerning plankton community changes. The most abundant microfossils in Panthalassic PTB sections are radiolarians, heterotrophic protists that live primarily in ocean-surface waters (<100 m water depth) but with sporadic occurrences to ~1000 m (Ishitani et al., 2008). Radiolarians were subject to rapid fluctuations in abundance during the latest Permian followed by a population crash at the PTB, a pattern attributed to reduced nutrient availability linked to environmental disturbances or climate change (Kakuwa, 1996; Beauchamp and Baud, 2002; Isozaki et al., 2007). The present study confirms the decimation of radiolarians during the PTB crisis, as shown by decreases in the biogenic silica flux of 4–5X at Gujo-Hachiman and ~2X at Ubara (see Sections 4.2 and 5.1). However, paleoproductivity proxy data for the present study sections imply that primary productivity in the mid-Panthalassic Ocean was stable or increased during the PTB crisis (see above). Thus, the decimation of radiolarians in this region is unlikely to have been related to limited nutrient availability (cf. Rampino and Caldeira, 2005), and other factors such as environmental stress (e.g., high temperatures, low dissolved [O_2], or episodic euxinia) must be invoked. Alternatively (or additionally), the shift from eukaryotic to prokaryotic phytoplankton communities (Grice et al., 2005; Xie et al., 2007; Cao et al., 2009) may have proved harmful to radiolarians. Radiolarians did not begin to recover in terms of diversity or biomass until the Spathian substage of the Early Triassic, about 2 Myr after the PTB crisis (Kakuwa, 1996; Kozur, 1998), perhaps in response to an amelioration of hostile environmental conditions and/or further changes in the composition of phytoplankton communities.

5.4. Spatial variation in the Panthalassic Ocean

The observations and inferences above provide constraints on the paleogeographic and paleoenvironmental conditions of the two study sites. Both were located in peri-equatorial areas of the Panthalassic Ocean during the Late Permian–Early Triassic (Fig. 1C). Ubara was probably located somewhat more proximally to continents or island arcs than Gujo-Hachiman, based on its 2–3X higher illite fluxes (Fig. 11B). Ubara shows evidence of higher primary productivity levels than Gujo-Hachiman, especially in their respective black shale facies, as adjudged from Ba_{xs} and P concentrations (see Section 5.3). This observation suggests that Ubara was located closer to the equatorial divergence zone (probably ± 5°), which is associated with elevated primary productivity (Murray and Leinen, 1993), and that Gujo-Hachiman was somewhat more distant from it (Fig. 12). However, radiolarian productivity was somewhat lower at Ubara than at Gujo-Hachiman based on biogenic silica fluxes (Fig. 11A), possibly due to spatial variation in the composition of the zooplankton community (cf. Kakuwa, 2008) or perhaps to environmental conditions less conducive to radiolarians at Ubara than at Gujo-Hachiman. The latter possibility may be supported by the alternation of gray chert and black shale layers through a ~1-m interval at Ubara (unit II), which records pronounced environmental fluctuations at timescales of tens of thousands of years for an interval of ~200–250 kyr during the Late Permian during which repeated decimation and (partial) recovery of the radiolarian community occurred.

Inferences of higher primary productivity at Ubara than at Gujo-Hachiman are consistent with patterns of redox variation between the two study sites. Benthic redox conditions (as inferred from DOP and trace-metal data; see Section 5.2) were generally more reducing at Ubara than at Gujo-Hachiman, which would have been a natural consequence of a higher sinking flux of organic matter in the water column at the former site (Fig. 12). Further, as benthic redox conditions deteriorated during the latest Permian, Ubara bottom waters went from suboxic to weakly anoxic whereas Gujo-Hachiman bottom waters went from oxic to suboxic, indicating a parallel shift toward more reducing conditions. Redox conditions higher in the water column (i.e., within the intermediate-depth OMZ) also differed between the study sites, as adjudged by fluxes of syngenetic framboidal pyrite (see Section 5.2). The OMZ at Ubara was already intermittently euxinic during the Late Permian (unit II) at a time when the equivalent units at Gujo-Hachiman (upper unit I and unit II) show no evidence of euxinia (i.e., a lack of framboidal pyrite; Fig. 3). As oceanic redox conditions deteriorated during the latest Permian, the OMZ at Gujo-Hachiman finally also went euxinic (unit III). These observations suggest the following model: euxinic conditions first appeared within the OMZ of the equatorial Panthalassic Ocean, developing intermittently in response to Milankovitch-band climate cycles for an interval of ~200–250 kyr during the Late Permian (equivalent to unit II of Ubara), followed by establishment of more permanently euxinic conditions that expanded to encompass a larger region north and south of the equator during the latest Permian (equivalent to the unit II–III contact of both sections).

Spatial variation in redox conditions within the Panthalassic Ocean, especially at shallower depths, has implications for patterns of biotic extinction, survival, and recovery during the PTB crisis. The sharper decline in biogenic silica fluxes at Gujo-Hachiman relative to Ubara (see Section 5.1) can be understood in the context of the more abrupt transition from suboxic to euxinic conditions in the OMZ of the former section (see above). The reappearance of many warm-water forms at the end of the Early Triassic or the beginning of the Middle Triassic suggests that these organisms must have occupied refugia for several million years following the PTB mass extinction event (Kozur, 1998). Many of these “Lazarus taxa” had lifestyles conducive to survival under low-oxygen conditions (Bottjer et al., 2008). Spatially variable redox conditions in the Panthalassic Ocean may have provided refugia for some of these taxa, aiding their survival and subsequent recovery.

6. Conclusions

The Ubara section was located within the high-productivity equatorial divergence zone of the central Panthalassic Ocean during the Late Permian to Early Triassic. High levels of primary productivity led to strongly reducing and intermittently euxinic conditions in the intermediate water mass (i.e., OMZ) and suboxic to weakly anoxic conditions at the seafloor. Euxinia in the OMZ intensified repeatedly during the ~200–250 kyr interval represented by unit II, causing episodic decimation and recovery of the radiolarian community at this site. The Gujo-Hachiman section was located at low latitudes, but not on the paleoequator, and at greater distance from continental sources of detrital siliciclastics than the Ubara section. Moderate levels of primary productivity were insufficient to produce euxinia at this site during most of the Late Permian, when gray cherts record sedimentation under suboxic bottomwaters. Expansion of euxinic conditions in the OMZ of the central Panthalassic Ocean during the latest Permian resulted in a mass kill-off of radiolarians and a transition from chert-to-black shale deposition at Gujo-Hachiman (i.e., unit II–III contact). The results of the present study (1) document major changes in marine primary productivity rates and plankton community composition in conjunction with the PTB boundary crisis, and (2) demonstrate that the most pronounced changes in redox conditions of the Panthalassic Ocean occurred within the OMZ rather than in the deep ocean.

Acknowledgments

Thanks to Valerie Owens and Ryan Wilson for assistance with sample processing, to Ron Blakely for generating a Panthalassa-centered paleogeographic map, and to Margaret Fraiser, David Kidder, and an anonymous reviewer for constructive reviews of the manuscript. Research by TJA was supported by grants from the National Science Foundation (EAR-0310072, EAR-0618003, and EAR-0745574) and the University of Cincinnati Research Council. This paper is a contribution to IGCP Project 572.

References

Algeo, T.J., Ingall, E.D., 2007. Sedimentary C_{org}:P ratios, paleocean ventilation, and Phanerozoic atmospheric pO_2. Palaeogeography Palaeoclimatology Palaeoecology 256, 130–155.
Algeo, T.J., Tribovillard, N., 2009. Environmental analysis of paleoceanographic systems based on molybdenum-uranium covariation. Chemical Geology 268, 211–225.
Algeo, T.J., Twitchett, R.J., 2010. Anomalous Early Triassic sediment fluxes due to elevated weathering rates and their biological consequences. Geology 38, 1023–1026.
Algeo, T.J., Shen, Y., Zhang, T., Lyons, T., Bates, S., Rowe, H., Nguyen, T.K.T., 2008. Association of ^{34}S-depleted pyrite layers with negative carbonate δ^{13}C excursions at the Permian–Triassic boundary: evidence for upwelling of sulfidic deep-ocean water masses. Geochemistry Geophysics Geosystems 9, Q04025. doi:10.1029/2007GC001823 10 pp.
Algeo, T.J., Hinnov, L., Moser, J., Maynard, J.B., Elswick, E., Kuwahara, K., Sano, H., 2010. Changes in productivity and redox conditions in the Panthalassic Ocean during the latest Permian. Geology 38, 187–190. doi:10.1130/G30483.1.
Ando, A., Kodama, K., Kojima, S., 2001. Low-latitude and Southern Hemispere origin of Anisian (Triassic) bedded chert in the Inuyama area, Mino terrane, central Japan. Journal of Geophysical Research 106 (B2), 1973–1986.
Bambach, R.K., Knoll, A.H., Wang, S.C., 2004. Origination, extinction, and mass depletions of marine diversity. Paleobiology 30, 522–542.
Beauchamp, B., Baud, A., 2002. Growth and demise of Permian biogenic chert along northwest Pangea: evidence for end-Permian collapse of thermohaline circulation. Palaeogeography Palaeoclimatology Palaeoecology 184, 37–63.
Berelson, W.M., Anderson, R.F., Dymond, J., DeMaster, D., Hammond, D.E., Collier, R., Honjo, S., Leinen, M., McManus, J., Pope, R., Smith, C., Stephens, M., 1997. Biogenic budgets of particle rain, benthic remineralization and sediment accumulation in the Equatorial Pacific. Deep-Sea Research (II) 44, 2251–2282.
Berner, R.A., 1972. Sulfate reduction, pyrite formation, and the oceanic sulfur budget. In: Dyrssen, D., Jagner, D. (Eds.), The Changing Chemistry of the Oceans, Nobel Symposium 20. Almqvist & Wiksell Förlag, Stockholm, pp. 347–361.
Berner, R.A., Raiswell, R., 1983. Burial of organic carbon and pyrite sulfur in sediments over Phanerozoic time: a new theory. Geochimica et Cosmochimica Acta 47, 855–862.
Blain, S., Leynaert, A., Tréguer, P., Chrétiennot-Dinet, M.-J., Rodier, M., 1997. Biomass, growth rates and limitation of equatorial Pacific diatoms. Deep-Sea Research (I) 44, 1255–1275.
Böning, P., Brumsack, H.-J., Böttcher, M.E., Schnetger, B., Kriete, C., Kallmeyer, J., Borchers, S.L., 2004. Geochemistry of Peruvian near-surface sediments. Geochimica et Cosmochimica Acta 68, 4429–4451.
Bottjer, D.J., Clapham, M.E., Fraiser, M.L., Powers, C.M., 2008. Understanding mechanisms for the end-Permian mass extinction and the protracted Early Triassic aftermath and recovery. GSA Today 18 (9), 4–10.
Bottrell, S.H., Newton, R.J., 2006. Reconstruction of changes in global sulfur cycling from marine sulfate isotopes. Earth-Science Reviews 75, 59–83.
Bragin, N.J., 1991. Radiolaria and Lower Mesozoic units of the USSR east regions. Nauka, Moscow. 125 pp. (in Russian with English abstract).
Brüchert, V., 1998. Early diagenesis of sulfur in estuarine sediments: the role of sedimentary humic and fulvic acids. Geochimica et Cosmochimica Acta 62, 1567–1586.
Canfield, D.E., Raiswell, R., Westrich, J.T., Reaves, C.M., Berner, R.A., 1986. The use of chromium reduction in the analysis of reduced inorganic sulfur in sediments and shales. Chemical Geology 54, 149–155.
Cao, C., Love, G.D., Hays, L.E., Wang, W., Shen, S., Summons, R.E., 2009. Biogeochemical evidence for euxinic oceans and ecological disturbance presaging the end-Permian mass extinction event. Earth and Planetary Science Letters 281, 188–201.
Dale, A.W., Brüchert, V., Alperin, M., Regnier, P., 2009. An integrated sulfur isotope model for Namibian shelf sediments. Geochimica et Cosmochimica Acta 73, 1924–1944.
Dehairs, F., Baeyens, W., Goeyens, L., 1992. Accumulation of suspended barite at mesopelagic depths and export production in the Southern Ocean. Science 258, 1332–1335.
Ellwood, B.B., Crick, R.R., El Hassani, A., Benoist, S.L.R.H., Young, R.H., 2000. The magnetosusceptibility event and cyclostratigraphy (MSEC) method applied to marine rocks: detrital input versus carbonate productivity. Geology 28, 1134–1138.
Erwin, D.H., 1994. The Permo-Triassic extinction. Nature 367, 231–236.
Grice, K., Cao, C., Love, G.D., Böttcher, M.E., Twitchett, R.J., Grosjean, E., Summons, R.E., Turgeon, S.C., Dunning, W., Jin, Y., 2005. Photic zone euxinia during the Permian–Triassic superanoxic event. Science 307, 706–709.
Grim, R.E., 1968. Clay Mineralogy, 2nd ed. McGraw-Hill, New York. 596 pp.
Gylesjö, S., 2005. Data report: Late Pleistocene terrigenous input to Shatsky Rise, Site 1208. In: Bralower, T.J., Premoli Silva, I., Malone, M.J. (Eds.), Proc. Ocean Drilling Program, Sci. Results, vol. 198. 7 pp. [online].
Hallam, A., Wignall, P.B., 1997. Mass Extinctions and Their Aftermath. Oxford University Press, Oxford. 320 pp.
Handbook of Chemistry and Physics, 85th ed. CRC Press, Boca Raton, Florida.
Hinnov, L.A., 2000. New perspectives on orbitally forced stratigraphy. Annual Review of Earth and Planetary Sciences 28, 419–475.
Hotinski, R.M., Bice, K.L., Kump, L.R., Najjar, R.G., Arthur, M.A., 2001. Ocean stagnation and end-Permian anoxia. Geology 29, 7–10.
Huey, R.B., Ward, P.D., 2005. Hypoxia, global warming, and terrestrial late Permian extinctions. Science 308, 398–401.
Ishiga, H., Ishida, K., Sampei, Y., Musashino, M., Yamakita, S., Kajiwara, Y., Morikiyo, T., 1993. Oceanic pollution at the Permian–Triassic boundary in pelagic condition from carbon and sulfur stable isotopic excursion, Southwest Japan. Bulletin of the Geological Survey of Japan 44, 721–726.
Ishitani, Y., Takahashi, K., Okazaki, Y., Tanaka, S., 2008. Vertical and geographic distribution of selected radiolarian species in the North Pacific. Micropaleontology 54, 27–39.
Isozaki, Y., 1994. Superanoxia across the Permo-Triassic boundary: record in accreted deep-sea pelagic chert in Japan. In: Embry, A.F., Beauchamp, B., Glass, D.J. (Eds.), Pangea: Global Environment and Resources: Canadian Society of Petreoleum Geologists Memoir, 17, pp. 805–812.
Isozaki, Y., 1997a. Jurassic accretion tectonics of Japan. The Island Arc 6, 25–51.
Isozaki, Y., 1997b. Triassic boundary superanoxia and stratified superocean: records from lost deep sea. Science 276, 235–238.
Isozaki, Y., 2007. A unique carbon isotope record across the Guadalupian–Lopingian (Middle-Upper Permian) boundary in mid-oceanic paleo-atoll carbonates: The high-productivity “Kamura event” and its collapse in Panthalassa. Global and Planetary Change 55, 21–38.
Isozaki, Y., Shimizu, N., Yao, J., Ji, Z., Matsuda, T., 2007. End-Permian extinction and volcanism-induced environmental stress: Permian–Triassic boundary interval of a lower-slope facies at Chaotian, South China. Palaeogeography Palaeoclimatology Palaeoecology 252, 218–238.
Kajiwara, Y., Yamakita, S., Ishida, K., Ishiga, H., Imai, A., 1994. Development of a largely anoxic stratified ocean and its temporary massive mixing at the Permian/Triassic boundary supported by the sulfur isotope record. Palaeogeography Palaeoclimatology Palaeoecology 111, 367–379.
Kakuwa, Y., 1996. Permian–Triassic mass extinction event recorded in bedded chert sequence in southwest Japan. Palaeogeography Palaeoclimatology Palaeoecology 121, 35–51.
Kakuwa, Y., 2008. Evaluation of palaeo-oxygenation of the ocean bottom across the Permian–Triassic boundary. Global and Planetary Change 63, 40–56.
Karl, S.M., Wandless, G.A., Karpoff, A.M., 1992. Sedimentological and geochemical characteristics of Leg 129 siliceous deposits. In: Larson, R.L., Lancelot, Y., et al. (Eds.), Proc. Ocean Drilling Program, Sci. Res., vol. 129, pp. 31–79.
Kato, Y., Nakao, K., Isozaki, Y., 2002. Geochemistry of Late Permian to Early Triassic pelagic cherts from southwest Japan: implications for an oceanic redox change. Chemical Geology 182, 15–34.
Kemp, A.E.S., Pearce, R.B., Grigorov, I., Rance, J., Lange, C.B., Quilty, P., Salter, I., 2006. Production of giant marine diatoms and their export at oceanic frontal zones: implications for Si and C flux from stratified oceans. Global Biogeochemical Cycles 20, GB4S04 13 pp.
Kenig, F., Hudson, J.D., Sinninghe Damsté, J.S., Popp, B.N., 2004. Intermittent euxinia: reconciliation of a Jurassic black shale with its biofacies. Geology 32, 421–424.
Kiehl, J.T., Shields, C.A., 2005. Climate simulation of the latest Permian: implications for mass extinction. Geology 33, 757–760.
Kienast, S.S., Kienast, M., Jaccard, S., Calvert, S.E., François, R., 2006. Testing the silica leakage hypothesis with sedimentary opal records from the eastern equatorial Pacific over the last 150 kyr. Geophysical Research Letters 33, L15607 4 pp.
Kimura, K., Makimoto, H., Yoshioka, T., 1989. Geology of the Ayabe district, Quadrangle Series scale 1:50,000. Geological Survery of Japan. 104 pp.
Kojima, S., 1989. Mesozoic terrane accretion in northeast China, Sikhote–Alin and Japan regions. Palaeogeography Palaeoclimatology Palaeoecology 69, 213–232.
Kozur, H.W., 1998. Some aspects of the Permian–Triassic boundary (PTB) and of the possible causes for the biotic crisis around this boundary. Palaeogeography Palaeoclimatology Palaeoecology 143, 227–272.
Kuwahara, K., 1997. Paleontological study of Late Permian Albaillella (Radiolaria). Journal of Geosciences, Osaka City University 40, 15–36.
Kuwahara, K., Yao, A., 2001. Late Permian radiolarian faunal change in bedded chert of the Mino Belt, Japan. News of Osaka Micropaleontologists 12, 33–49 (in Japanese).
Kuwahara, K., Nakae, S., Yao, A., 1991. Late Permian “Toishi-type” siliceous mudstone in the Mino–Tamba Belt. Journal of the Geological Society of Japan 97, 1005–1008 (in Japanese).
Kuwahara, K., Yao, A., Yamakita, S., 1998. Reexamination of Upper Permian radiolarian biostratigraphy. “Earth Science” (Chikyu Kagaku) 52, 391–404.
Lefticariu, L., Pratt, L.M., Ripley, E.M., 2006. Mineralogic and sulfur isotopic effects accompanying oxidation of pyrite in millimolar solutions of hydrogen peroxide at temperatures from 4 to 150 °C. Geochimica et Cosmochimica Acta 70, 4889–4905.

Levitus, S., Boyer, T., 1994. World Ocean Atlas 1994, Volume 2: Oxygen. NOAA Atlas NESDIS, vol. 2. U.S. Department of Commerce, Washington, D.C. (http://iridl.ldeo.columbia.edu/sources/.levitus94/.annual/.O2/).

Matsuda, T., Isozaki, Y., 1991. Well-documented travel history of Mesozoic pelagic chert in Japan: from remote ocean to subduction zone. Tectonics 10, 475–499.

Matsuo, M., Kubo, K., Isozaki, Y., 2003. Mössbauer spectroscopic study on characterization of iron in the Permian to Triassic deep-sea chert from Japan. Hyperfine Interaction (C)5, 435–438.

McGee, D., Marcantonio, F., Lynch-Stieglitz, J., 2007. Deglacial changes in dust flux in the eastern equatorial Pacific. Earth and Planetary Science Letters 257, 215–230.

McManus, J., Berelson, W.M., Klinkhammer, G.P., Johnson, K.S., Coale, K.H., Anderson, R.F., Kumar, N., Buridge, D.J., Hammond, D.E., Brumsack, H.J., McCorkle, D.C., Rushdi, A., 1998. Geochemistry of barium in marine sediments: implications for its use as a paleoproxy. Geochimica et Cosmochimica Acta 62, 3453–3473.

Mizutani, S., 1987. Mesozoic terranes in the Japanese Islands and neighbouring East Asia. In: Scheibner, E. (Ed.), Terrane Accretion and Orogenic Belts: American Geophysical Union, Geodynamics Series, 19, pp. 263–273.

Molinie, A.J., Ogg, J.G., 1992. Milankovitch cycles in Upper Jurassic and Lower Cretaceous radiolarites of the equatorial Pacific: spectral analysis and sedimentation rate curves. In: Larson, R.L., Lancelot, Y., et al. (Eds.), Proc. Ocean Drilling Program, Sci. Res., vol. 129, pp. 529–547.

Monger, J.W.H., Wheeler, J.O., Tipper, H.W., Gabrielse, H., Harms, T., Struik, L.C., Campbell, R.B., Dodds, C.J., Gehrels, G.E., O'Brien, J., 1991. Part B. Cordilleran terranes. In: Gabrielse, H., Yorath, C.J. (Eds.), Geology of the Cordilleran Orogen in Canada. Geology of Canada, no. 4. Geological Survey of Canada, Ottawa, pp. 281–327.

Mundil, R., Pálfy, J., Renne, P.R., Brack, P., 2010. The Triassic time scale: new constraints and a review of geochronological data. In: Lucas, S.G. (Ed.), The Triassic Timescale: Geological Society of London, Special Publication, 334, pp. 41–60.

Murray, R.W., Leinen, M., 1993. Chemical transport to the seafloor of the equatorial Pacific Ocean across a latitudinal transect at 135°W: tracking sedimentary major, trace, and rare earth element fluxes at the Equator and the Intertropical Convergence Zone. Geochimica et Cosmochimica Acta 57, 4141–4163.

Musashi, M., Isozaki, Y., Koike, T., Kreulen, R., 2001. Stable carbon isotope signature in mid-Panthalassa shallow-water carbonates across the Permo-Triassic boundary: evidence for ^{13}C-depleted ocean. Earth and Planetary Science Letters 196, 9–20.

Nakajima, T., 1997. Regional metamorphic belts of the Japanese islands. The Island Arc 6, 69–90.

Nielson, J.K., Shen, Y., 2004. Evidence for sulfidic deep water during the Late Permian in the East Greenland Basin. Geology 32, 1037–1040.

Ogg, J.G., Karl, S.M., Behl, R.J., 1992. Jurassic through Early Cretaceous sedimentation history of the central equatorial Pacific and of Sites 800 and 801. In: Larson, R.L., Lancelot, Y., et al. (Eds.), Proc. Ocean Drilling Program, Sci. Res., vol. 129, pp. 571–613.

Okazaki, Y., Takahashi, K., Asahi, H., 2008. Temporal fluxes of radiolarians along the W–E transaction in the central and western equatorial Pacific, 1999–2002. Micropaleontology 54, 71–86.

Olivarez-Lyle, A., Lyle, M., 2006. Organic carbon and barium in Eocene sediments: possible controls on nutrient recycling in the Eocene Equatorial Pacific Ocean. In: Wilson, P.A., Lyle, M., Firth, J.V. (Eds.), Proc. Ocean Drilling Program, Sci. Res., vol. 199. 33 pp. [online].

Paillard, D., Labeyrie, L., Yiou, P., 1996. Macintosh program performs time-series analysis. EOS 77, 379.

Pondaven, P., Ragueneau, O., Tréguer, P., Hauvespre, A., Dezileau, L., Reyss, J.L., 2000. Resolving the 'opal paradox' in the Southern Ocean. Nature 405, 168–172.

Raiswell, R., Berner, R.A., 1985. Pyrite formation in euxinic and semi-euxinic sediments. American Journal of Science 285, 710–724.

Raiswell, R., Berner, R.A., 1987. Organic carbon losses during burial and thermal maturation of normal marine shales. Geology 15, 853–856.

Raiswell, R., Buckley, F., Berner, R.A., Anderson, T.F., 1988. Degree of pyritization of iron as a paleoenvironmental indicator of bottom-water oxygenation. Journal of Sedimentary Petrology 58, 812–819.

Rampino, M.R., Caldeira, K., 2005. Major perturbation of ocean chemistry and a 'Strangelove Ocean' after the end-Permian mass extinction. Terra Nova 17, 554–559.

Rea, D.K., Janacek, T.R., 1981. Mass-accumulation rates of the non-authigenic inorganic crystalline (eolian) component of deep-sea sediments from the western Mid-Pacific Mountains, Deep Sea Drilling Project Site 463. Init. Repts. Deep Sea Drilling Project, vol. 62. U.S. Govt. Printing Office, Washington, D.C., pp. 653–659.

Riccardi, A., Arthur, M.A., Kump, L.R., 2006. Sulfur isotopic evidence for chemocline upward excursions during the end-Permian mass extinction. Geochimica et Cosmochimica Acta 70, 5740–5752.

Sano, H., Nakashima, K., 1997. Lowermost Triassic (Griesbachian) microbial bindstone–cementstone facies, southwest Japan. Facies 36, 1–24.

Schaffer, G., Olsen, S.M., Pedersen, J.O.P., 2009. Long-term ocean oxygen depletion in response to carbon dioxide emissions from fossil fuels. Nature Geoscience 2, 105–109.

Schlager, W., 2005. Carbonate Sedimentology and Sequence Stratigraphy, SEPM Concepts in Sedimentology and Paleontology Series no. 8. Society for Sedimentary Geology (SEPM-SSG), Tulsa, Oklahoma. 200 pp.

Scotese, C.R., Langford, R.P., 1995. Pangea and the paleogeography of the Permian. In: Scholle, P.A., Peryt, T.M., Ulmer-Scholle, D.S. (Eds.), The Permian of Northern Pangeaa. Paleogeography, Paleoclimates, Stratigraphy, vol. 1. Springer-Verlag, Berlin, pp. 3–19.

Sheldon, N.D., 2006. Abrupt chemical weathering increase across the Permian–Triassic boundary. Paleogeography Palaeoclimatology Paleoecology 231, 315–321.

Shibuya, H., Sasajima, S., 1986. Paleomagnetism of red cherts: a case study in the Inuyama area, central Japan. Geochemical Journal 16, 213–223.

Stampfli, G.M., Borel, G.D., 2001. A plate tectonic model for the Paleozoic and Mesozoic constrained by dynamic plate boundaries and restored synthetic oceanic isochrones. Earth and Planetary Science Letters 196, 17–33.

Strauss, H., 1997. The isotopic composition of sedimentary sulfur through time. Paleogeography Palaeoclimatology Paleoecology 132, 97–118.

Sugiyama, K., 1992. Lower and Middle Triassic radiolarians from Mt. Kinkazan, Gifu Prefecture, central Japan. Transactions and Proceedings of the Palaeontological Society of Japan, New Ser., no. 167, pp. 1180–1223.

Suzuki, N., Ishida, K., Shinomiya, Y., Ishiga, H., 1998. High productivity in the earliest Triassic ocean: black shales, Southwest Japan. Palaeogeography Palaeoclimatology Palaeoecology 141, 53–65.

Swartzendruber, L.J., 1992. Properties, units and constants in magnetism. Journal of Magnetic Materials 100, 573–575.

Takemura, A., Sakai, M., Sakamoto, S., Aono, R., Takemura, S., Yamakita, S., 2007. Earliest Triassic radiolarians from the ARH and ARF sections on Arrow Rocks, Waipapa Terrane, Northland, New Zealand. In: Sporli, K.B., Takemura, A., Hori, R.S. (Eds.), The Oceanic Permian/Triassic Boundary Sequence at Arrow Rocks (Oruatemanu) Northland, New Zealand: GNS Science Monography, 24, pp. 97–107. Lower Hutt, New Zealand.

Taylor, S.R., McLennan, S.M., 1985. The Continental Crust: Its Composition and Evolution. Blackwell Scientific Publications, Oxford.

Thiede, J., Rea, D.K., 1981. Mass-accumulation rates of Barremian to Recent biogenic sediments from the Mid-Pacific Mountains (Deep Sea Drilling Project Site 463) and Hess Rise (Sites 464, 465, and 466), central North Pacific Ocean. Deep Sea Drilling Project, Init. Results, v. 62, pp. 637–651.

Tomczak, M., Godfrey, J.S., 2005. Regional Oceanography: An Introduction, PDF version 1.1 (online: www.es.flinders.edu.au/~mattom/regoc/pdfversion.html).

Tréguer, P., Nelson, D.M., Van Bennekom, A.J., DeMaster, D.J., Leynaert, A., Queguiner, B., 1995. The silica balance in the world ocean: a reestimate. Science 268, 375–379.

Virgili, C., 2008. The Permian–Triassic transition; historical review of the most important ecological crises with special emphasis on the Iberian Peninsula and western–central Europe. Journal of Iberian Geology 34, 123–158.

Wignall, P.B., 2007. The End-Permian mass extinction—how bad did it get? Geobiology 5, 303–309.

Wignall, P.B., Twitchett, R.J., 1996. Oceanic anoxia and the end-Permian mass extinction. Science 272, 1155–1158.

Wignall, P.B., Twitchett, R.J., 2002. Extent, duration, and nature of the Permian–Triassic superanoxic event. In: Koeberl, C., MacLeod, K.G. (Eds.), Catastrophic Events and Mass Extinctions: Impacts and Beyond: Geological Society of America Special Paper, 356, pp. 395–413.

Wignall, P.B., Newton, R., Brookfield, M.E., 2005. Pyrite framboid evidence for oxygen-poor deposition during the Permian–Triassic crisis in Kashmir. Palaeogeography Palaeoclimatology Palaeoecology 216, 183–188.

Wilkin, R.T., Arthur, M.A., 2001. Variations in pyrite texture, sulfur isotope composition, and iron systematics in the Black Sea; evidence for late Pleistocene to Holocene excursions of the O_2-H_2S redox transition. Geochimica et Cosmochimica Acta 65, 1399–1416.

Wilkin, R.T., Barnes, H.L., Brantley, S.L., 1996. The size distribution of framboidal pyrite in modern sediments: an indicator of redox conditions. Geochimica et Cosmochimica Acta 60, 3897–3912.

Winguth, A.M.E., Maier-Reimer, E., 2005. Causes of marine productivity and oxygen changes associated with the Permian–Triassic boundary: a reevalution with ocean general circulation models. Marine Geology 217, 283–304.

Xie, S., Pancost, R.D., Huang, X., Jiao, D., Lu, L., Huang, J., Yang, F., Evershed, R.P., 2007. Molecular and isotopic evidence for episodic environmental change across the Permo/Triassic boundary at Meishan in South China. Global and Planetary Change 55, 56–65.

Xiong, Z., Li, T., Algeo, T., Nan, Q., Zhai, B., Lu, B., submitted for publication. Major and trace metals and biogenic components of diatom mats from tropical West Pacific: implications for redox conditions and paleoproductivity. Marine Geology, submitted December 2009.

Yamakita, S., Kadota, N., Kato, T., Tada, R., Ogihara, S., Tajika, E., Hamada, Y., 1999. Confirmation of the Permian/Triassic boundary in deep-sea sedimentary rocks; earliest Triassic conodonts from black carbonaceous claystone of the Ubara section in the Tamba Belt, Southwest Japan. Journal of the Geological Society of Japan 105, 895–898.

Yamakita, S., 1987. Stratigraphic relationship between Permian and Triassic strata of chert facies in the Chichibu Terrane in eastern Shikoku. Journal of the Geological Society of Japan 93, 145–148 (in Japanese).

Yao, J., Yao, A., Kuwahara, K., 2001. Upper Permian biostratigraphic correlation between conodont and radiolarian zones in the Tamba–Mino Terrane, southwest Japan. Journal of Geosciences, Osaka City University 44, 97–119.

Yao, A., Kuwahara, K., Ezaki, Y., Liu, J., Hao, W., Luo, Y., Kuang, G., 2005. Permian and Triassic radiolarians from the western Guangxi area, China. Journal of Geosciences, Osaka City University 48, 81–93.